Heterophily-informed Message Passing

Anonymous authors
Paper under double-blind review

Abstract

Graph neural networks (GNNs) are known to be vulnerable to oversmoothing due to their implicit homophily assumption. We mitigate this problem with a novel scheme that regulates the aggregation of messages, modulating the type and extent of message passing locally thereby preserving both the low and high-frequency components of information. Our approach relies solely on learnt embeddings, obviating the need for auxiliary labels, thus extending the benefits of heterophily-aware embeddings to broader applications, e.g. generative modelling. Our experiments, conducted across various data sets and GNN architectures, demonstrate performance enhancements and reveal heterophily patterns across standard classification benchmarks. Furthermore, application to molecular generation showcases notable performance improvements on chemoinformatics benchmarks.

1 Introduction

Methods for ubiquitous graph-structured data with abundant topological information have advanced the field of graph representation learning in recent years. Graph neural networks (GNNs) have emerged as prominent deep learning models in this domain (Hamilton, 2020). A key feature of GNNs is the message-passing (MP) scheme—inspired by belief propagation—which facilitates the processing of local topology while maintaining computational efficiency (Dai et al., 2016). The MP scheme enables local information exchange between nodes and their neighbours; implicitly assuming strong *homophily*, *i.e.*, the tendency of nodes to connect with others that have similar labels or features. This assumption turns out to be reasonable in settings such as social data (McPherson et al., 2001), regional planning (Gerber et al., 2013), and citation networks (Ciotti et al., 2016). However, heterophilous graphs exist in many scenarios, *e.g.*, in fraud transaction networks (Pandit et al., 2007) and actor co-occurrence networks (Tang et al., 2009). They violate the homophily assumption, leading to sub-optimal performance (Zhu et al., 2020; 2021; Chien et al., 2021; Lim et al., 2021; Wang et al., 2023), owing to *oversmoothing* (Li et al., 2018) resulting from flattening of high-frequency information (Wu et al., 2023) by MP schemes.

A conceptual way to characterize homophily is by examining the neighbours of each node in a graph. For example, in a graph representing a molecule a fully *homophilous* molecule only has links between atoms of the same type, while a *heterophilous* molecule has links between different types. However, in practice, node labels necessary for homophily calculation are often missing due to lack of information or unavailable due to privacy concerns. Instead, heterophily typically stems from more intricate properties of the graph which need to be learned from data. For this problem, we introduce a general heterophily-informed MP scheme to carefully address and utilize the heterophily properties in graph data.

Many previous works analyze the impact of heterophily on GNN performance and design innovative structures to mitigate it (Zhu et al., 2020; Liu et al., 2021a; Yan et al., 2022; Ma et al., 2021). Some studies offer deeper insights into how heterophily affects model expressiveness (Ma et al., 2021; Luan et al., 2022; Mao et al., 2023; Luan et al., 2023). However, most of these works provide a specialized model and only focus on simple node classification tasks. In contrast, we aim to design a simple yet flexible structure that can be applied to any GNN. We verify its effectiveness not only on classification tasks but also more challenging molecular generation tasks, which require models to learn the data distribution on graph embeddings.

Our contributions We introduce a novel heterophily-informed MP scheme, serving as an approach for general GNNs to utilize data heterophily, designed to learn graph structures and node features across varying

degrees of homophily and heterophily. The scheme improves various GNN architectures for node classification in different domains of data. Furthermore, we apply our approach to a flow-based graph generation model (HetFlows). Our key contributions are summarized below:

- **Conceptual and technical:** We propose an architecture-independent approach that encodes homophily/heterophily patterns for general GNNs with flexible applications and highlights the necessity of data heterophily as the model prior.
- **Methodological:** We design a heterophily-informed message-passing scheme focusing on specific node heterophily patterns and apply it to *(i)* various classic GNNs for node classification and *(ii)* an invertible flow-based model (HetFlows) for molecule generation.
- **Empirical:** We demonstrate the benefits of our idea by benchmarking node classification accuracy and in molecule generation by evaluating the generated molecules with an extensive set of chemoinformatics metrics.

Notable advantages of our model include enhancing performance on different graph learning tasks without adding extra parameters, offering flexible applications across various GNN architectures, and revealing the homophily pattern match between message passing and data sets.

2 Related Work

Graph heterophily Graph heterophily refers to the connectivity tendency among nodes with diffferent labelings, as the opposed of graph homophily. This property could be measured by node homophily (Pei et al., 2019), edge homophily (Zhu et al., 2020) or more dedicated designed metrics (Lim et al., 2021; Platonov et al., 2024). Recent research shows the importances and benefits of considering heterophily in graph learning. For example, Empirical experiments (Zhu et al., 2022) show heterophilic nature in stucture attacks, and validate that heterophily incorporation enhances model robustness to adversarial attacks. Similarly to oversmoothing, the heterophily challenges graph learning by less discriminative node representation, Bodnar et al. (2022) links the GNN performances in heterophilic graphs with the oversmoothing problem by celluar sheaf theory.

Heterophily-awared GNNs Numerous techniques have been developed to address degradation in the performance of GNNs in heterophilic settings. Some approaches expand the concept of neighbour sets, such as aggregating messages from farther hops of neighbours (Abu-El-Haija et al., 2019; Wang & Derr, 2021) or searching for potential new neighbours (Pei et al., 2019; Jin et al., 2021; Li et al., 2022). Other focus on refining the message during the aggregation process, such as differentiating neighbours through specific filters (Luan et al., 2021; Yan et al., 2022; Wang et al., 2023) or collecting embeddings from previous layers, like jumping knowledge (Xu et al., 2018) and generalized PageRank techniques (Chien et al., 2021). These methods typically require additional parameters or specialized structures to achieve their effects. However, we hope to capture the effects with minimal modifications (no additional parameters), making the solution flexible and widely applicable. Heterophily-informed MP can be viewed as performing adaptive message modulation before aggregation.

Molecule representation and generation Early works in molecule generation (Kusner et al., 2017; Guimaraes et al., 2017; Gómez-Bombarelli et al., 2018; Dai et al., 2018) primarily used sequence models to encode the SMILES (short for 'Simplified Molecular-Input Line-Entry System') strings (Weininger et al., 1989), posing generation as an autoregressive problem. However, the mapping from molecules to SMILES is not continuous, so similar molecules can be assigned vastly different string representations. Graphs provide an elegant abstraction to encode the interactions between the atoms in a molecule. Thus the field has gravitated towards representing molecules as (geometric) graphs and using powerful graph encoders; *e.g.*, based on graph neural networks (GNNs), for example, adversarial models (De Cao & Kipf, 2018; You et al., 2018), energy-based models (Liu et al., 2021b), diffusion models (Hoogeboom et al., 2022; Xu et al., 2023), Neural ODEs (Verma et al., 2022) and flow-based models (Shi et al., 2019; Luo et al., 2021; Zang & Wang, 2020).

3 Heterophily-informed Message Passing

We propose an architecture-independent approach that encodes homophily/heterophily patterns for general GNNs, and later apply it to GNNs in node classification and graph generation setups.

3.1 Prerequisites: Message Passing

Graph Neural Networks (GNNs) have emerged as a potent paradigm for learning from graph-structured data, where the challenges include diverse graph sizes and varying structures (Kipf & Welling, 2017; Veličković et al., 2018; Xu et al., 2019; Garg et al., 2020). Consider a graph $G = (\mathcal{V}, \mathcal{E})$ with nodes $\mathcal{V}$ and edges $\mathcal{E}$. For these nodes and edges, we denote the corresponding node features as $\boldsymbol{X} = \{\boldsymbol{x}_v \in \mathbb{R}^{n_a} \mid v \in \mathcal{V}\}$ and edge features as $\boldsymbol{E} = \{\boldsymbol{e}_{uv} \in \mathbb{R}^{n_b} \mid u, v \in \mathcal{E}\}$. Here n_a, n_b are the feature dimensions of nodes and edges. For each node $v \in \mathcal{V}$, its embedding at the kth layer is represented as $\boldsymbol{h}_v^{(k)}$, and $\boldsymbol{h}^{(k)} = \{\boldsymbol{h}_v^{(k)} \mid v \in \mathcal{V}\}$. These embeddings evolve through a sequence of transformations across GNNs of depth K, by the message passing scheme (Hamilton, 2020):

$$\boldsymbol{m}_{uv}^{(k)} = \text{MESSAGE}^{(k)}\left(\boldsymbol{h}_u^{(k)}, \boldsymbol{e}_{uv}\right), \quad u \in \mathcal{N}(v), \tag{1}$$

$$\boldsymbol{h}_v^{(k+1)} = \text{UPDATE}^{(k)}\left(\boldsymbol{h}_v^{(k)}, \boldsymbol{m}_{\mathcal{N}(v)}^{(k)}\right), \tag{2}$$

for $k \in \{0, 1, \ldots, K\}$. Here $\mathcal{N}(v)$ denotes the neighbour set of node v. Both $\text{UPDATE}^{(k)}$ and $\text{MESSAGE}^{(k)}$ are arbitrary differentiable functions. Messages from all neighbours of v are aggregated in the multiset $\boldsymbol{m}_{\mathcal{N}(v)}^{(k)} = \{\{\boldsymbol{m}_{uv}^{(k)} \mid u \in \mathcal{N}(v)\}\}$. Importantly, the function $\text{UPDATE}^{(k)}$ needs to be permutation invariant on this message set $\boldsymbol{m}_{\mathcal{N}(v)}^{(k)}$ (*e.g.*, by resorting to operations like summation or taking the maximum). However, in practice, a naïve aggregation strategy typically mixes messages, especially in heterophilic areas, leading to the 'oversmoothing' problem (Zhu et al., 2020; 2021; Chien et al., 2021; Lim et al., 2021; Wang et al., 2023).

3.2 Heterophily-informed Message Passing

Our method encodes the heterophily assumption into the MP scheme of the GNN, denoted as $\text{GNN}^{\gamma}(\boldsymbol{X} \mid \boldsymbol{E}) = \boldsymbol{h}^{(K)}$. The indicator $\gamma \in \Gamma = \{\text{orig.}, \text{hom.}, \text{het.}\}$ specifies the heterophily preference of the GNNs: whether they lean towards homophily (hom.), heterophily (het.), and original structure (orig.). The $\text{GNN}^{\text{orig.}}$ is exactly the original GNN described at Sec. 3.1. And we name $\text{GNN}^{\text{het.}}$ and $\text{GNN}^{\text{hom.}}$ after the HetMP and HomMP modes of $\text{GNN}^{\text{orig.}}$. Referring to Eq. (1) and Eq. (2), the messages undergo different scaling preprocessing steps before being sent forward to the subsequent layer:

$$\boldsymbol{m}_{uv}^{(k)} = \text{MESSAGE}^{(k)}\left(\boldsymbol{h}_u^{(k)}, \boldsymbol{e}_{uv}\right), \quad u \in \mathcal{N}(v), \tag{3}$$

$$\boldsymbol{m}_{\mathcal{N}(v)}^{(k)} = \{\{\alpha_{uv,\gamma}^{(k)} \boldsymbol{m}_{uv}^{(k)} \mid u \in \mathcal{N}(v)\}\}, \tag{4}$$

$$\boldsymbol{h}_v^{(k+1)} = \text{UPDATE}^{(k)}\left(\boldsymbol{h}_v^{(k)}, \boldsymbol{m}_{\mathcal{N}(v)}^{(k)}\right), \tag{5}$$

where the scaling factors

$$\alpha_{uv,\gamma}^{(k)} = \begin{cases} \mathcal{H}(u,v), & \text{if } \gamma = \text{hom.} \\ 1, & \text{if } \gamma = \text{orig.} \\ 1 - \mathcal{H}(u,v), & \text{if } \gamma = \text{het.} \end{cases} \tag{6}$$

and $\mathcal{H}$ denotes the homophily of the node (Pei et al., 2019) and the embeddings initilized by $\boldsymbol{h}^{(0)} = \boldsymbol{X}$. Aiming to learn embeddings as node labels, therefore in practice, instead of traditional label-style definition in many contexts, we define the homophily or *attraction to similarity* between embeddings as the cosine similarity $\mathcal{H}(u,v) \triangleq S_{\cos}(\boldsymbol{h}_u^{(k)}, \boldsymbol{h}_v^{(k)})$ at the relevant layer.

The message passing process of an example GNN and its HetMP, HomMP versions are visualized in Fig. 1 as three channels. The input is an example molecule 3-Aminophenol, and node colouring corresponds to the embeddings while similar colour means closer embeddings. The thickness of the bond corresponds to the

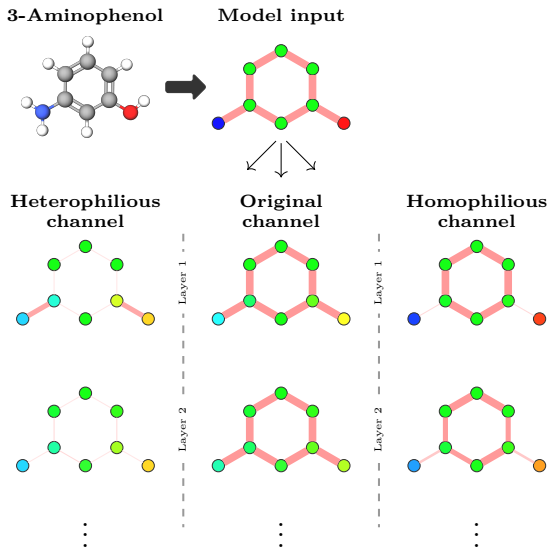

Figure 1: Comparison of heterophiliy-informed MP with original GNN on a graph describing the 3-Aminophenol molecule. The three channels show how γ controls the scaling factor in Eq. (6) and lead to different message passing behaviour, given the same input.

scaling factor α_γ (which shows the similarity between node pairs) of the last layer. The homophilous channels (hom.) decrease information exchange between dissimilar neighbours, introducing frictions during message flows. The heterophilous channel (het.) encourages faster message spreading on higher frequency locality, while slowing it down when neighbors become similar. In this simple example, the original channel (orig.) shows the typical oversmoothing issue: all the node embeddings become similar after layers, while the other two channels (homophilous/heterophilous channels) mitigate it with different convergence resistances, thus improving model effectiveness.

3.3 Application to Molecular Generation

For generative modelling on molecule graphs, we propose a graph-generation model leveraging normalizing flows based on heterophily-informed MP: HetFlows. Our model is split into two main components: a bond flow and a atom flow. The bond flow learns the molecular topology, while the atom flow assigns certain atomic details to this structure.

Prerequisites In general, **normalizing flows** offer a methodological approach to model distributions based on the change-of-variable law of probabilities. This is achieved by applying a chain of reversible and bijective transformations between trivial variables (like Gaussians) with target data variables and updating the transformation to minimize the negative log-likelihood (Dinh et al., 2014).

Affine coupling layers (ACLs) introduce reversible transformations to normalizing flows, ensuring efficient computation of the log-determinant of the Jacobian (Kingma & Dhariwal, 2018). ALCs keep reversibility by updating partial information via the other part of the information. Series of ACLs $\{f_1, \ldots, f_T\}$ build a reversible flow between the Gaussian with the target distribution $f = f_T \circ \cdots \circ f_1$.

Training and loss Given molecule graph $G = (\boldsymbol{X}, \boldsymbol{E})$, the atom flow f_a and bond flow f_b map the graph into embeddings which follow Gaussian distributions $\mathcal{N}_a, \mathcal{N}_b$:

$$f_a(\boldsymbol{X}|\boldsymbol{E}) = \boldsymbol{h}_a \sim \mathcal{N}_a, \quad f_b(\boldsymbol{E}) = \boldsymbol{h}_b \sim \mathcal{N}_b. \tag{7}$$

The model is trained to minimize the negative log-likelihoods (NLLs) of the data by gradient descent. The target loss function of the model $\mathcal{L}$ could be decomposed into two parts since HetFlows contains two flows

$\mathcal{L} = \mathcal{L}_a + \mathcal{L}_b$. The atom loss $\mathcal{L}_a$ is defined as following

$$\mathcal{L}_a = -\log p_X(\boldsymbol{X}) = -\log p\left(\boldsymbol{h}_a\right) - \log\det\left(\left|\frac{\partial f_a}{\partial \boldsymbol{X}}\right|\right). \tag{8}$$

The bond loss $\mathcal{L}_b$ is defined similarly as above.

Generation process Given a trained model f_{a*}, f_{b*} with established parameters, sampled embeddings randomly from Gaussian $\boldsymbol{h}_a, \boldsymbol{h}_b \sim \mathcal{N}_a, \mathcal{N}_b$. Then the embeddings can generate features of bonds $\boldsymbol{E} = f_{b*}^{-1}(\boldsymbol{h}_b)$ and atoms $\boldsymbol{X} = f_{a*}^{-1}(\boldsymbol{h}_a|\boldsymbol{E})$ in sequence, which requires the reversibility of flow model. Finally, the molecules are reconstructed $G = (\boldsymbol{X}, \boldsymbol{E})$. Additionally, the bond features generation can be achieved by sampling the adjacency matrix from the real data distribution which reflects the model separability.

The HetFlows shares the same structure of MoFlow (Zang & Wang, 2020): ACL-based normalizing flows. The coupling function stores most parameters of an ACL, serving as the most essential part. The main difference between these two methods is the message passing scheme of GNN utilized as coupling functions in all ACLs of flow: MoFlow contains the classical graph convolutional networks (Kipf & Welling, 2017), and the HetFlows substitute it with a heterophily informed version. This GNN processes input with three modes of GCN: original, HetMP, HomMP, and then merge them together.

Further details of HetFlows are discussed in App. A, including introductions of normalizing flows and ACLs, mathematical model description, the training and generation process of HetFlows, the loss function, and a proof of model reversibility.

4 Experiments

We demonstrate the effects of heterophily-informed MP both in discriminative node classification benchmarks and molecule generation settings. Sec. 4.1 compares the node classification performances of various types of GNNs with their variants (HetMP and HomMP versions) across 12 data sets. In Sec. 4.2, we demonstate how our multi-channel MP GNN blocks improve flow-based molecule generation, directly showing the benefits of our MP scheme.

4.1 Node Classification Benchmarks

Data sets The node classification experiments belong to the class of semi-supervised learning tasks. We evaluated on 6 homophilic data sets in citation networks (Yang et al., 2016) (Cora, PubMed, CiteSeer), co-purchase graphs (Shchur et al., 2018) (Computers, Photo), and a co-author network (Shchur et al., 2018) (CoauthorCS). Furthermore, the 6 heterophilic data sets including hyperlink networks (Pei et al., 2019) (Cornell, Wisconsin, Texas), Wikipedia networks (Rozemberczki et al., 2021) (Chameleon, Squirrel), and actor co-occurrence network (Tang et al., 2009) (Actor). The summary statistics of all data sets mentioned above are listed in Table A4.

Settings The data split settings (training/validation/test = 60%/20%/20%) follow those in GEOM-GCN (Pei et al., 2019). Each configuration (data set and model) is tested for 100 random model initializations and data splits.

Baselines Four different GNN architectures are chosen as baseline models: Graph Convolutional Network (GCN) (Kipf & Welling, 2017), Graph Attention Network (GAT) (Veličković et al., 2018), Graph Isomorphism Network (GIN) (Xu et al., 2019), and GraphSAGE (Hamilton et al., 2017). For more details about the data split rules and base GNNs, please refer to App. B.

Implementation The models were implemented in PyTorch (Paszke et al., 2019) and PyTorch Geometric (PyG) (Fey & Lenssen, 2019). The base model GNNs in Sec. 4.1 are the PyG-implemented versions. Each one and its variants (HetMP, HomMP) contain 4 layers and 128 dimensions for all hidden layers. The HetFlows in Sec. 4.2 is built on GNNs with 4 layers and flows that were $k_a = 27, k_b = 10$ (for QM9) deep

Table 1: We shed light on how our homo-/heterophilous message passing can boost standard node classification benchmark accuracy (mean±std). Data sets are sorted according to their homophily level. For each data (column), four classic GNN architectures (GCN, GAT, GIN, GraphSAGE) are tested, grouped with their corresponding HetMP/HomMP modes (with +hom. or +hom.). Numbers are bolded with a paired t-test (5% significance level) for each 3 mode group. Our MP methods perform either equally well or significantly better in all cases, except for homophilic data sets with GAT—**in 44/48 of the combinations**.

Homophily $\mathcal{H}_n$	Texas 0.10	Cornell 0.11	Wisconsin 0.13	Actor 0.21	Squirrel 0.22	Chameleon 0.25	CiteSeer 0.71	Computers 0.79	PubMed 0.79	Cora 0.83	CoauthorCS 0.83	Photo 0.84
GCN	**58.6**±5.7	41.1±4.7	**51.4**±6.0	**26.7**±1.7	**27.2**±1.2	37.1±1.9	**75.8**±1.4	**88.8**±1.4	85.5±0.5	**87.2**±0.9	92.2±0.6	**92.9**±0.5
GCN+hom.	**59.5**±5.8	40.5±5.3	**51.0**±7.0	**26.4**±1.4	**27.4**±1.4	**38.0**±2.3	**76.5**±1.5	**88.7**±1.1	**86.6**±0.6	**87.3**±1.2	**92.6**±0.6	**92.7**±0.8
GCN+het.	**58.4**±5.7	**48.1**±8.2	**46.3**±8.4	25.0±1.3	**28.3**±1.9	26.7±1.9	57.0±2.3	68.0±1.6	82.5±0.8	73.9±2.5	79.8±3.8	**86.3**±10.9
GAT	**58.4**±5.3	**40.8**±5.8	**52.0**±8.0	**27.4**±0.9	**28.3**±1.2	**41.8**±2.8	**75.5**±1.5	**90.3**±0.6	85.4±0.4	**86.1**±1.2	**91.1**±0.5	**93.3**±0.6
GAT+hom.	57.0±4.1	**43.2**±5.6	**52.5**±5.9	**27.6**±1.0	**28.3**±1.4	**41.2**±2.5	**75.8**±1.7	89.8±0.5	**86.5**±0.7	84.8±1.0	90.4±0.5	92.6±0.3
GAT+het.	**59.7**±5.3	**44.6**±6.9	**48.4**±8.0	25.4±1.2	26.6±1.2	24.8±2.6	52.8±2.4	66.6±7.8	78.6±1.6	62.7±2.7	51.6±11.0	68.8±6.4
GIN	**54.9**±9.1	**40.8**±4.5	43.7±8.4	24.7±1.3	**25.4**±4.6	26.2±6.2	**63.8**±11.3	39.2±3.0	**73.8**±18.3	**82.9**±2.5	38.6±27.1	26.3±4.7
GIN+hom.	52.2±8.6	**44.3**±8.9	**43.9**±5.9	**26.9**±1.3	**24.4**±5.7	**29.3**±7.3	**68.4**±2.7	38.1±1.9	**71.8**±22.2	**82.5**±2.6	65.6±31.2	25.7±2.4
GIN+het.	**57.3**±5.7	**46.2**±9.0	**48.8**±8.3	**27.9**±2.1	**26.6**±3.2	**33.0**±5.1	**65.9**±4.2	**62.2**±11.0	**73.8**±18.4	79.4±4.0	**90.4**±0.7	**78.5**±17.4
GraphSAGE	**65.4**±8.5	**60.3**±9.0	62.4±9.4	34.1±0.7	36.3±1.6	**47.2**±2.3	75.3±0.8	**90.8**±0.4	87.9±0.4	**87.4**±0.8	93.2±0.5	**95.5**±0.5
GraphSAGE+hom.	**62.4**±7.3	**60.5**±6.1	**65.1**±7.6	**35.5**±1.1	**37.1**±1.5	**47.6**±3.0	**76.3**±1.1	**90.9**±0.5	**88.5**±0.5	**86.9**±0.8	93.6±0.5	**95.4**±0.3
GraphSAGE+het.	**65.1**±5.2	**59.5**±9.2	**69.6**±6.5	34.3±1.2	36.1±1.6	**48.0**±2.9	**75.4**±1.1	88.4±0.6	86.7±0.6	85.2±1.7	**94.6**±0.3	94.3±0.7

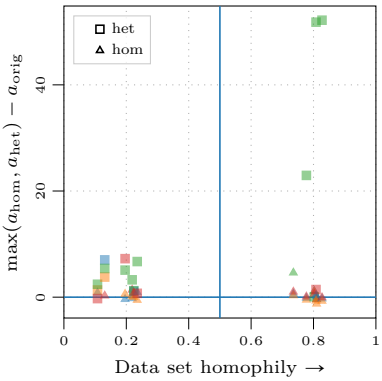

(a) Accuracy improvement of HetMP and HomMP

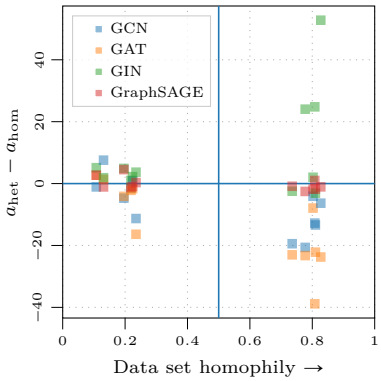

(b) Comparison between HetMP and HomMP

Figure 2: Comparison over 12 data sets and 4 GNN architectures in terms of improvement in accuracy (%-points). a_{orig}, a_{hom} and a_{het} denote the accuracy of original model and corresponding HetMP and HomMP versions. In Fig. 2a, each node is the average performance over 100 random seeds for specific dataset and GNN structure. The x-axis denotes the homophily level of experiment data, and the y-axis denotes the maximum average accuracy improvement of HetMP and HomMP over original structure (triangle means HomMP better, square reverse). Fig. 2b illustrates the accuracy advantage of HetMP above HomMP.

and $k_a = 38, k_b = 10$ (for ZINC-250K). All the models are trained with the AdamW optimizer (Loshchilov & Hutter, 2019) and learning rate 0.001. For the generation task, we select the best-performing model using the FCD score as suggested in Polykovskiy et al. (2020).

Results The comprehensive benchmark results in Table 1 include the node classification accuracy (each value representing the average of 100 random runs) of the four base models and their HetMP and HomMP versions across 12 different graph domains, with data homophily displayed. For each GNN and data set, the best result among the three modes is highlighted in bold. For more intuitive visualizations, Fig. 2 illustrates the benefits of classification accuracy on heterophily-informed MP and special patterns through the accuracy discrepancies between HomMP and HetMP modes.

Analysis Table 1 shows that for the 6 heterophilic data sets, our MP schemes perform as well or better then the baseline (in 24 out of 24 cases). In the 6 homophilic data sets, our methods perform either equally well or significantly better for GCN, GIN, and GraphSage, with GAT being the exception. In Fig. 2a, most points are on or above the y-axis, which shows that the heterophily-informed MP scheme brings node classification performance enhancement. The performance improvement on these various combinations implies the potential

generalization capability of our approach, which could also be applied to a wider range of GNN structures and data domains. Furthermore, the HetMP or HomMP scheme only modifies the message passing without requiring abundant prior knowledge or additional parameters.

In Fig. 2b, the accuracy difference $a_{\text{het.}} - a_{\text{hom.}}$ of HomMP over HetMP is concentrated in the top-left and bottom-right regions. Compared with HomMP, the HetMP is beneficial to heterophilic data ($\mathcal{H}$ lower than 0.5) and harmful to the homophilic data. This provides strong evidence about the implicit homophily assumption under the MP scheme and show the strong pattern between the data homophily level and model preference. In conclusion, our model modification is able to incorporate the data heterophily as structural prior knowledge.

Based on the figures and tables above, the GIN model demonstrates the most significant improvement when applying our heterophily-informed MP. This improvement is likely due to the straightforward design of MP, which offers a high degree of flexibility and strong sensitivity to the heterophily prior (as shown in App. B.3). However, this flexibility also results in greater variance in GIN's performance compared to other GNNs, making it an outlier in the pattern discussed in the previous paragraph. On the other hand, the GAT model shows limited performance improvement on homophilic data sets, possibly because its attention mechanism is less compatible with our MP adjustments.

In conclusion, the node classification experiment shows the capability of HetMP/HomMP to incorporate data homophily prior and enhance node-level graph representation learning.

4.2 Molecule Generation

Molecules express varying levels of homo-/heterophily. Thus molecular modelling provides an interesting benchmark for our proposed MP scheme. We demonstrate the impact of accounting for heterophilic message passing in a variety of common benchmark tasks for molecule generation and modelling. We provide results for molecule generation with benchmarks on a wide range of chemoinformatics metrics.

Data sets We consider two common molecule data sets: QM9 and ZINC-250K. The QM9 data set (Ramakrishnan et al., 2014) comprises ∼134k stable small organic molecules composed of atoms from the set {C, H, O, N, F}. These molecules have been processed into their kekulized forms with hydrogens removed using the RDkit software (Landrum et al., 2013). The ZINC-250K (Irwin et al., 2012) data contains ∼250k drug-like molecules, each with up to 38 atoms of 9 different types.

Chemoinformatics metrics We compare methods through an extensive set of chemoinformatics metrics that perform both sanity checks (validity, uniqueness, and novelty) on the generated molecule corpus and quantify properties of the molecules: neighbour (SNN), fragment (Frag), and scaffold (Scaf) similarity, internal diversity (IntDiv_1 and IntDiv_2), and Fréchet ChemNet distance (FCD). We also show score histograms and distribution distances for solubility (logP), synthetic accessibility (SA), drug-likeness (QED), and molecular weight. For computing the metrics, we use the MOSES benchmarking platform (Polykovskiy et al., 2020) and the RDKit open-source cheminformatics software (Landrum et al., 2013). The 'data' row in metrics is based on averages over 10 randomly sampled sets (1000 mols per set) from the data. For the metrics, we simulate 10 batches of 1000 mols and compare them to a hold-out reference set (20% of data, other 80% used for training). Full details on the 14 metrics we use are included in App. D.

Baselines For random generation, we include baseline results for methods that have pre-trained models publicly available. Trained models are required for generating chemoinformatics metrics beyond trivial sanity checks (validity, uniqueness, and novelty). We compare GraphDF (Luo et al., 2021) and MoFlow (Zang & Wang, 2020) which are current state-of-the-art flow models for molecular generation.

Results on QM9 For the QM9 data set, the main chemoinformatic summary statistics are given in Table 2 and the descriptive distributions in Fig. 3. HetFlows +true adj. achieves best validity, SNN Frag and Scaf, especially lowest FCD over flow-based models. Full benchmark results are available in the extended listings in Table A5 in the Appendix.

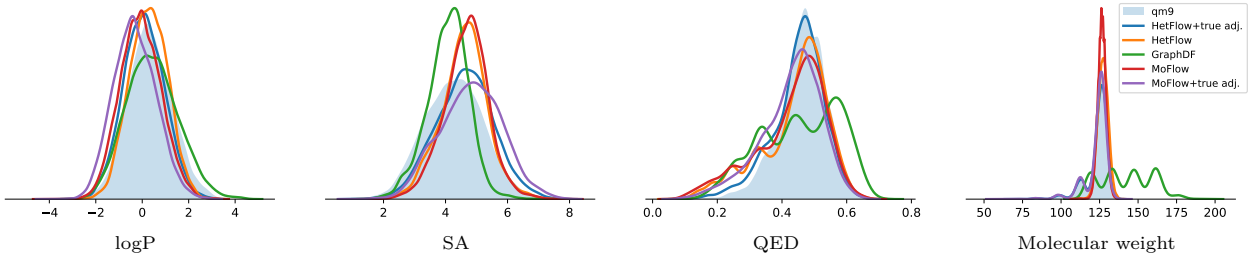

Figure 3: Chemoinformatics statistics for data (QM9) and generated molecules from HetFlows (ours), MoFlow, and GraphDF. We report histograms for the Octanol-water partition coefficient (logP), synthetic accessibility score (SA), quantitative estimation of drug-likeness (QED), and molecular weight.

Table 2: Chemoinformatics summary statistics for random generation on the QM9 molecule data. Full listing of all 14 metrics in Table A5. '+true adj.' means the adjacency matrices are sampled from the real (data) distribution. The results show that our message passing modification of MoFlow (resulting in HetFlows) achieves better results on FCD, SNN, Frag, and Scaf, and retains competitive performance on other metrics.

		FCD ↓	Validity ↑	Novelty ↑	SNN ↑	Frag ↑	Scaf ↑	IntDiv_1 ↑
	Data (QM9)	0.40	1.00±0.00	0.62±0.02	0.54±0.00	0.94±0.01	0.76±0.03	0.92±0.00
Flows	GraphDF	10.76	-	**0.98**±0.00	0.35±0.00	0.61±0.01	0.09±0.07	0.87±0.00
	MoFlow	7.55	0.95±0.01	0.96±0.01	0.32±0.00	0.60±0.03	0.04±0.03	**0.92**±0.00
	HetFlow (Ours)	4.04	0.92±0.01	0.92±0.01	0.34±0.00	0.80±0.02	0.04±0.03	0.91±0.00
Abl.	MoFlow+true adj.	4.45	**1.00**±0.00	0.85±0.01	0.38±0.00	0.70±0.03	0.31±0.08	**0.92**±0.00
	HetFlow+true adj.	**1.46**	**1.00**±0.00	0.74±0.01	**0.43**±0.00	**0.85**±0.02	**0.52**±0.05	**0.92**±0.00

Table 3: Chemoinformatics summary statistics for random generation on the ZINC-250K molecule data set. Full listing of all 14 metrics in Table A6. '+true adj.' means the adjacency matrices are sampled from the real (data) distribution.

		FCD ↓	Validity ↑	Novelty ↑	SNN ↑	Frag ↑	Scaf ↑	IntDiv_1 ↑
	Data (ZINC-250K)	1.44	1.00±0.00	0.02±0.00	0.51±0.00	1.00±0.00	0.28±0.02	0.87±0.00
Flows	GraphDF	34.30	-	**1.00**±0.00	0.23±0.00	0.35±0.01	0.00±0.00	**0.88**±0.00
	MoFlow	23.33	0.89±0.01	**1.00**±0.00	0.27±0.00	0.79±0.01	0.01±0.00	**0.88**±0.00
	HetFlow (Ours)	23.72	0.87±0.01	**1.00**±0.00	0.26±0.00	0.77±0.01	0.01±0.00	**0.88**±0.00
Abl.	MoFlow+true adj.	**8.21**	**0.94**±0.01	**1.00**±0.00	0.33±0.00	0.89±0.01	0.07±0.02	0.87±0.00
	HetFlow+true adj.	8.24	0.93±0.01	**1.00**±0.00	**0.34**±0.00	**0.91**±0.01	**0.10**±0.03	0.87±0.00

Results on ZINC-250K For the ZINC-250K data set, the main chemoinformatic summary statistics are given in Table 3 and the descriptive distributions in Fig. A7. While the ZINC-250K data set is more complicated, HetFlows +true adj. achieves the best Novelty SNN, Frag and Scaf, and has competitive performance on other metrics. Full benchmark results are available in the extended listings in Table A6.

Analysis HetFlows emerges as a robust and versatile molecular generation model, adept at balancing fidelity, diversity, and molecular properties. Notably, the validity on both QM9 and ZINC-250K are higher than 85%, ensuring the model's reliability. As discussed in Sec. 3.3, HetFlows is built based on the MoFlow (Zang & Wang, 2020). It replaces the classic graph convolution of the GCNs module of MoFlow with multi-channel message passing. In other words, the difference between MoFlow and HetFlows is the GNNs, more exactly, the MP scheme. As Table 2 and Table 3 show, HetFlows is superior over MoFlow with both adjacency matrix generation styles on QM9 and ZINC-250K. Fig. 3 shows the chemoinformatics statistics of generated molecules from HetFlows fit the original distribution better than MoFlow in both generation styles. It provides evidence of the advantage of utilizing the heterophily inside the message passing, as intuited by Fig. 1.

Visualizing the continuous latent space Inspired by Zang & Wang (2020), we examine the learned latent space of our method on both QM9 and ZINC-250K, presented in Fig. 4 and Fig. A6, respectively. Qualitatively,

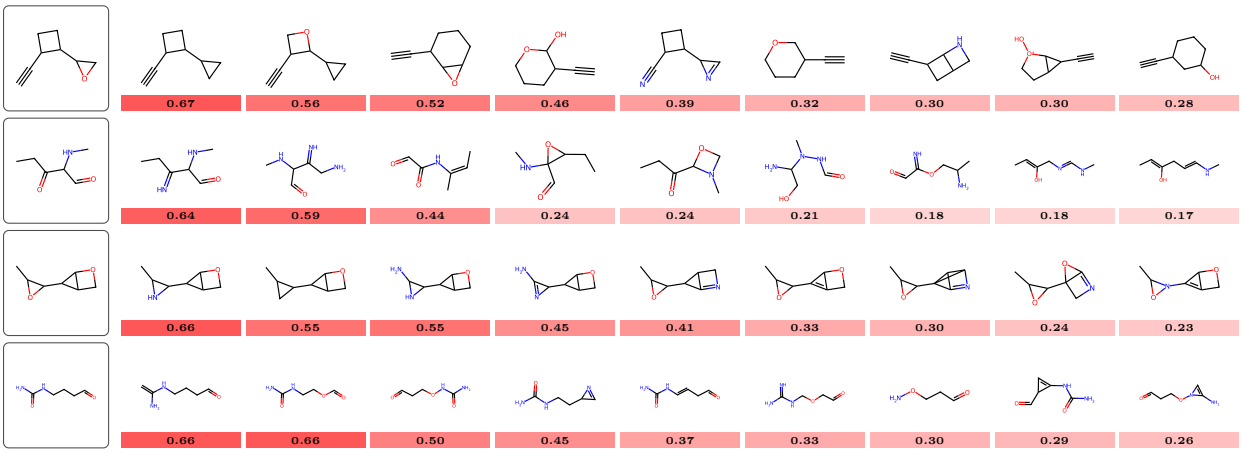

Figure 4: **Structured latent-space exploration (QM9).** Our approach yields a sensibly-structured latent space as qualitatively demonstrated by this nearest neighbour search in the latent space with the seed molecule on the left and neighbours with the Tanimoto similarity (1 0) given for each molecule. For results on ZINC-250K, see Fig. A6 in the appendix.

we note that the latent space appears smooth and the molecules near the seed molecule resemble the input and have high Tanimoto similarity (Rogers & Hahn, 2010).

4.3 Ablations Studies

To further verify that the effects we see are due to our proposed heterophily-informed MP scheme, we include ablation studies on different adjacency matrix generation strategies and parameter sharing of the GNNs.

Ablation study: adjacency matrix generation As mentioned in Sec. 3.3, the adjacency matrix can be generated by the bond model or sampled directly from the real distribution. Both approaches are present in literature as a basis for modelling (see, *e.g.*, discussion in Verma et al., 2022). With sampled adjacency matrices, the main task of the model is to put correct labels on a given graph topology. As the comparison results in Table 2 and Table 3 ('+true adj.') show, the adjacency matrix generated by the bond model limits the model generation performance compared with the sampling alternative. However, this approach can be considered a method of its own.

Ablation study: parameter sharing of heterophilous GNN There are three channels of message passing scheme as shown in Fig. 1, the three channels could share parameters or not, which corresponds to whether $\text{MESSAGE}_{\gamma}^{(k)}$ in Eq. (3) is the same function for all $\gamma \in \Gamma$ or not. To investigate the improved expressiveness of heterophilous GNNs from extra two channels, models with two settings are compared in Table A7 and Table A8. Based on the chemoinformatics metrics, the random generation outputs of the two settings are similar. It means the model strength stems from the more expressive structure as intuited by Fig. 1, not from the larger parameter size.

5 Conclusions and Discussion

We have presented a heterophily-informed message passing scheme, a flexible plug-in module of GNNs to account for a heterophily prior, countering the traditional oversmoothing vulnerability prevalent in existing GNN-based methodologies. By adjusting message passing to discern (dis-)similarities between nodes, our method offers a more nuanced representation of the intricate balance between affinities and repulsions without requiring additional parameters. In the experiments, we demonstrated our approach both in standard discriminative node classification benchmarks and by applying the approach inside a generative flow model (which we call HetFlows). Experiment results show the versatility and ability of the proposed scheme to enhance embedding expressiveness across multiple graph domains. The analysis underscores the necessity of

aligning data homophily with corresponding model assumptions. We consider this approach a promising tool in heterophilic graph learning.

One limitation of heterophily-informed MP is the variable effectiveness across different GNN architectures. As discussed in Sec. 4.1, the scheme brings limited advantages to the attention-aware architecture GAT. Meanwhile, the GIN, a well-known GNN type that maintains the abstract format of message passing and is theoretically proven to be expressive through the Weisfeiler–Lehman test (Xu et al., 2019), benefited most noticeably from our module. This observation encourages further analysis of homophily-induced modelling effects. It also suggests clear potential for improving various MP mechanisms. Such improvements could be achieved through better estimation of graph homophily and more intelligent integration of different channels.

In molecular generation, the dependency on the current adjacency matrix generation (bond model) method perhaps restricts HetFlows's effects, as the key coupling functions, based on CNNs, capture limited structural information. With a sampled adjacency matrix, it successfully generates molecules that are valid, novel, diverse, and chemoinformatically similar to those in the existing distribution.

The code and trained models will be made available under the MIT License on GitHub upon acceptance (see supplementary material for now).

References

Sami Abu-El-Haija, Bryan Perozzi, Amol Kapoor, Nazanin Alipourfard, Kristina Lerman, Hrayr Harutyunyan, Greg Ver Steeg, and Aram Galstyan. MixHop: Higher-order graph convolutional architectures via sparsified neighborhood mixing. In *Proceedings of the 36th International Conference on Machine Learning (ICML)*, volume 97 of *Proceedings of Machine Learning Research*, pp. 21–29. PMLR, 2019.

Cristian Bodnar, Francesco Di Giovanni, Benjamin Chamberlain, Pietro Lio, and Michael Bronstein. Neural sheaf diffusion: A topological perspective on heterophily and oversmoothing in gnns. *Advances in Neural Information Processing Systems*, 35:18527–18541, 2022.

Eli Chien, Jianhao Peng, Pan Li, and Olgica Milenkovic. Adaptive universal generalized pagerank graph neural network. In *International Conference on Learning Representations (ICLR)*, 2021.

Valerio Ciotti, Moreno Bonaventura, Vincenzo Nicosia, Pietro Panzarasa, and Vito Latora. Homophily and missing links in citation networks. *EPJ Data Science*, 5:1–14, 2016.

Hanjun Dai, Bo Dai, and Le Song. Discriminative embeddings of latent variable models for structured data. In *Proceedings of The 33rd International Conference on Machine Learning (ICML)*, volume 48 of *Proceedings of Machine Learning Research*, pp. 2702–2711. PMLR, 2016.

Hanjun Dai, Yingtao Tian, Bo Dai, Steven Skiena, and Le Song. Syntax-directed variational autoencoder for structured data. *arXiv preprint arXiv:1802.08786*, 2018.

Nicola De Cao and Thomas Kipf. MolGAN: An implicit generative model for small molecular graphs. *ICML 2018 Workshop on Theoretical Foundations and Applications of Deep Generative Models*, 2018.

Laurent Dinh, David Krueger, and Yoshua Bengio. Nice: Non-linear independent components estimation. *arXiv preprint arXiv:1410.8516*, 2014.

Matthias Fey and Jan E. Lenssen. Fast graph representation learning with PyTorch Geometric. In *ICLR Workshop on Representation Learning on Graphs and Manifolds*, 2019.

Vikas Garg, Stefanie Jegelka, and Tommi Jaakkola. Generalization and representational limits of graph neural networks. In *International Conference on Machine Learning (ICML)*, pp. 3419–3430. PMLR, 2020.

Elisabeth R Gerber, Adam Douglas Henry, and Mark Lubell. Political homophily and collaboration in regional planning networks. *American Journal of Political Science*, 57(3):598–610, 2013.

Rafael Gómez-Bombarelli, Jennifer N Wei, David Duvenaud, José Miguel Hernández-Lobato, Benjamín Sánchez-Lengeling, Dennis Sheberla, Jorge Aguilera-Iparraguirre, Timothy D Hirzel, Ryan P Adams, and Alán Aspuru-Guzik. Automatic chemical design using a data-driven continuous representation of molecules. *ACS Central Science*, 4(2):268–276, 2018.

Gabriel Lima Guimaraes, Benjamin Sanchez-Lengeling, Carlos Outeiral, Pedro Luis Cunha Farias, and Alán Aspuru-Guzik. Objective-reinforced generative adversarial networks (organ) for sequence generation models. *arXiv preprint arXiv:1705.10843*, 2017.

Will Hamilton, Zhitao Ying, and Jure Leskovec. Inductive representation learning on large graphs. In *Advances in Neural Information Processing Systems 30 (NIPS)*, pp. 1025–1035. Curran Associates, Inc., 2017.

William L Hamilton. *Graph Representation Learning*. Morgan & Claypool Publishers, 2020.

Emiel Hoogeboom, Vıctor Garcia Satorras, Clément Vignac, and Max Welling. Equivariant diffusion for molecule generation in 3d. In *International Conference on Machine Learning (ICML)*, pp. 8867–8887. PMLR, 2022.

John J Irwin, Teague Sterling, Michael M Mysinger, Erin S Bolstad, and Ryan G Coleman. ZINC: A free tool to discover chemistry for biology. *Journal of Chemical Information and Modeling*, 52(7):1757–1768, 2012.

Di Jin, Zhizhi Yu, Cuiying Huo, Rui Wang, Xiao Wang, Dongxiao He, and Jiawei Han. Universal graph convolutional networks. In *Advances in Neural Information Processing Systems 34 (NeurIPS)*, pp. 10654–10664. Curran Associates, Inc., 2021.

Wengong Jin, Regina Barzilay, and Tommi Jaakkola. Junction tree variational autoencoder for molecular graph generation. In *International Conference on Machine Learning (ICML)*, pp. 2323–2332. PMLR, 2018.

Durk P. Kingma and Prafulla Dhariwal. Glow: Generative flow with invertible 1x1 convolutions. In *Advances in Neural Information Processing Systems (NeurIPS)*, volume 31, pp. 10236–10245. Curran Associates, Inc., 2018.

Thomas N. Kipf and Max Welling. Semi-supervised classification with graph convolutional networks. In *International Conference on Learning Representations (ICLR)*, 2017.

Matt J Kusner, Brooks Paige, and José Miguel Hernández-Lobato. Grammar variational autoencoder. In *International Conference on Machine Learning (ICML)*, pp. 1945–1954. PMLR, 2017.

Greg Landrum et al. RDKit: A software suite for cheminformatics, computational chemistry, and predictive modeling. *Greg Landrum*, 8:31, 2013.

AA Leman and Boris Weisfeiler. A reduction of a graph to a canonical form and an algebra arising during this reduction. *Nauchno-Technicheskaya Informatsiya*, 2(9):12–16, 1968.

Qimai Li, Zhichao Han, and Xiao-Ming Wu. Deeper insights into graph convolutional networks for semi-supervised learning. In *Proceedings of the AAAI Conference on Artificial Intelligence*, volume 32, 2018.

Xiang Li, Renyu Zhu, Yao Cheng, Caihua Shan, Siqiang Luo, Dongsheng Li, and Weining Qian. Finding global homophily in graph neural networks when meeting heterophily. In *Proceedings of the 39th International Conference on Machine Learning (ICML)*, volume 162 of *Proceedings of Machine Learning Research*, pp. 13242–13256. PMLR, 2022.

Derek Lim, Felix Hohne, Xiuyu Li, Sijia Linda Huang, Vaishnavi Gupta, Omkar Bhalerao, and Ser Nam Lim. Large scale learning on non-homophilous graphs: New benchmarks and strong simple methods. In *Advances in Neural Information Processing Systems 34 (NeurIPS)*, pp. 20887–20902. Curran Associates, Inc., 2021.

Meng Liu, Zhengyang Wang, and Shuiwang Ji. Non-local graph neural networks. *IEEE Transactions on Pattern Analysis and Machine Intelligence*, 44(12):10270–10276, 2021a.

Meng Liu, Keqiang Yan, Bora Oztekin, and Shuiwang Ji. GraphEBM: Molecular graph generation with energy-based models. *arXiv preprint arXiv:2102.00546*, 2021b.

Ilya Loshchilov and Frank Hutter. Decoupled weight decay regularization. In *International Conference on Learning Representations (ICLR)*, 2019.

Sitao Luan, Chenqing Hua, Qincheng Lu, Jiaqi Zhu, Mingde Zhao, Shuyuan Zhang, Xiao-Wen Chang, and Doina Precup. Is heterophily a real nightmare for graph neural networks to do node classification? *arXiv preprint arXiv:2109.05641*, 2021.

Sitao Luan, Chenqing Hua, Qincheng Lu, Jiaqi Zhu, Mingde Zhao, Shuyuan Zhang, Xiao-Wen Chang, and Doina Precup. Revisiting heterophily for graph neural networks. In *Advances in Neural Information Processing Systems 35 (NeurIPS)*, pp. 1362–1375. Curran Associates, Inc., 2022.

Sitao Luan, Chenqing Hua, Minkai Xu, Qincheng Lu, Jiaqi Zhu, Xiao-Wen Chang, Jie Fu, Jure Leskovec, and Doina Precup. When do graph neural networks help with node classification: Investigating the homophily principle on node distinguishability. *arXiv preprint arXiv:2304.14274*, 2023.

Youzhi Luo, Keqiang Yan, and Shuiwang Ji. GraphDF: A discrete flow model for molecular graph generation. In *International Conference on Machine Learning (ICML)*, pp. 7192–7203. PMLR, 2021.

Yao Ma, Xiaorui Liu, Neil Shah, and Jiliang Tang. Is homophily a necessity for graph neural networks? *arXiv preprint arXiv:2106.06134*, 2021.

Haitao Mao, Zhikai Chen, Wei Jin, Haoyu Han, Yao Ma, Tong Zhao, Neil Shah, and Jiliang Tang. Demystifying structural disparity in graph neural networks: Can one size fit all? *arXiv preprint arXiv:2306.01323*, 2023.

Miller McPherson, Lynn Smith-Lovin, and James M Cook. Birds of a feather: Homophily in social networks. *Annual Review of Sociology*, 27(1):415–444, 2001.

Shashank Pandit, Duen Horng Chau, Samuel Wang, and Christos Faloutsos. Netprobe: A fast and scalable system for fraud detection in online auction networks. In *Proceedings of the 16th International Conference on World Wide Web*, WWW '07, pp. 201–210. Association for Computing Machinery, 2007. ISBN 9781595936547.

Adam Paszke, Sam Gross, Francisco Massa, Adam Lerer, James Bradbury, Gregory Chanan, Trevor Killeen, Zeming Lin, Natalia Gimelshein, Luca Antiga, et al. PyTorch: An imperative style, high-performance deep learning library. In *Advances in Neural Information Processing Systems 32 (NeurIPS)*, pp. 8026–8037. Curran Associates, Inc., 2019.

Hongbin Pei, Bingzhe Wei, Kevin Chen-Chuan Chang, Yu Lei, and Bo Yang. Geom-GCN: Geometric graph convolutional networks. In *International Conference on Learning Representations (ICLR)*, 2019.

Oleg Platonov, Denis Kuznedelev, Artem Babenko, and Liudmila Prokhorenkova. Characterizing graph datasets for node classification: Homophily-heterophily dichotomy and beyond. *Advances in Neural Information Processing Systems*, 36, 2024.

Daniil Polykovskiy, Alexander Zhebrak, Benjamin Sanchez-Lengeling, Sergey Golovanov, Oktai Tatanov, Stanislav Belyaev, Rauf Kurbanov, Aleksey Artamonov, Vladimir Aladinskiy, Mark Veselov, et al. Molecular sets (MOSES): A benchmarking platform for molecular generation models. *Frontiers in Pharmacology*, 11: 565644, 2020.

Raghunathan Ramakrishnan, Pavlo O Dral, Matthias Rupp, and O Anatole Von Lilienfeld. Quantum chemistry structures and properties of 134 kilo molecules. *Scientific Data*, 1(1):1–7, 2014.

David Rogers and Mathew Hahn. Extended-connectivity fingerprints. *Journal of Chemical Information and Modeling*, 50(5):742–754, 2010.

Benedek Rozemberczki, Carl Allen, and Rik Sarkar. Multi-scale attributed node embedding. *Journal of Complex Networks*, 9(2):cnab014, 2021.

Oleksandr Shchur, Maximilian Mumme, Aleksandar Bojchevski, and Stephan Günnemann. Pitfalls of graph neural network evaluation. *arXiv preprint arXiv:1811.05868*, 2018.

Chence Shi, Minkai Xu, Zhaocheng Zhu, Weinan Zhang, Ming Zhang, and Jian Tang. Graphaf: a flow-based autoregressive model for molecular graph generation. In *International Conference on Learning Representations (ICLR)*, 2019.

Jie Tang, Jimeng Sun, Chi Wang, and Zi Yang. Social influence analysis in large-scale networks. In *Proceedings of the 15th ACM SIGKDD international conference on Knowledge discovery and data mining*, pp. 807–816, 2009.

Petar Veličković, Guillem Cucurull, Arantxa Casanova, Adriana Romero, Pietro Liò, and Yoshua Bengio. Graph attention networks. *International Conference on Learning Representations (ICLR)*, 2018.

Yogesh Verma, Samuel Kaski, Markus Heinonen, and Vikas Garg. Modular flows: Differential molecular generation. In *Advances in Neural Information Processing Systems 35 (NeurIPS)*, pp. 12409–12421. Curran Associates, Inc., 2022.

Yu Wang and Tyler Derr. Tree decomposed graph neural network. In *Proceedings of the 30th ACM International Conference on Information & Knowledge Management*, CIKM '21, pp. 2040–2049. Association for Computing Machinery, 2021.

Yuelin Wang, Kai Yi, Xinliang Liu, Yu Guang Wang, and Shi Jin. ACMP: Allen-Cahn message passing with attractive and repulsive forces for graph neural networks. In *International Conference on Learning Representations (ICLR)*, 2023.

David Weininger, Arthur Weininger, and Joseph L Weininger. SMILES. 2. Algorithm for generation of unique SMILES notation. *Journal of Chemical Information and Computer Sciences*, 29(2):97–101, 1989.

Lirong Wu, Haitao Lin, Bozhen Hu, Cheng Tan, Zhangyang Gao, Zicheng Liu, and Stan Z Li. Beyond homophily and homogeneity assumption: Relation-based frequency adaptive graph neural networks. *IEEE Transactions on Neural Networks and Learning Systems*, 2023.

Keyulu Xu, Chengtao Li, Yonglong Tian, Tomohiro Sonobe, Ken-ichi Kawarabayashi, and Stefanie Jegelka. Representation learning on graphs with jumping knowledge networks. In *Proceedings of the 35th International Conference on Machine Learning (ICML)*, volume 80 of *Proceedings of Machine Learning Research*, pp. 5453–5462. PMLR, 2018.

Keyulu Xu, Weihua Hu, Jure Leskovec, and Stefanie Jegelka. How powerful are graph neural networks? In *International Conference on Learning Representations (ICLR)*, 2019.

Minkai Xu, Alexander S Powers, Ron O. Dror, Stefano Ermon, and Jure Leskovec. Geometric latent diffusion models for 3D molecule generation. In *Proceedings of the 40th International Conference on Machine Learning (ICML)*, volume 202 of *Proceedings of Machine Learning Research*, pp. 38592–38610. PMLR, 2023.

Yujun Yan, Milad Hashemi, Kevin Swersky, Yaoqing Yang, and Danai Koutra. Two sides of the same coin: Heterophily and oversmoothing in graph convolutional neural networks. In *IEEE International Conference on Data Mining (ICDM)*, pp. 1287–1292. IEEE, 2022.

Zhilin Yang, William Cohen, and Ruslan Salakhudinov. Revisiting semi-supervised learning with graph embeddings. In *Proceedings of The 33rd International Conference on Machine Learning (ICML)*, volume 48 of *Proceedings of Machine Learning Research*, pp. 40–48. PMLR, 2016.

Jiaxuan You, Bowen Liu, Zhitao Ying, Vijay Pande, and Jure Leskovec. Graph convolutional policy network for goal-directed molecular graph generation. In *Advances in Neural Information Processing Systems 31 (NeurIPS)*, pp. 6410–6421. Curran Associates, Inc., 2018.

Chengxi Zang and Fei Wang. Moflow: An invertible flow model for generating molecular graphs. In *Proceedings of the 26th ACM SIGKDD International Conference on Knowledge Discovery & Data Mining*, pp. 617–626, 2020.

Jiong Zhu, Yujun Yan, Lingxiao Zhao, Mark Heimann, Leman Akoglu, and Danai Koutra. Beyond homophily in graph neural networks: Current limitations and effective designs. In *Advances in Neural Information Processing Systems 33 (NeurIPS)*, pp. 7793–7804. Curran Associates, Inc., 2020.

Jiong Zhu, Ryan A Rossi, Anup Rao, Tung Mai, Nedim Lipka, Nesreen K Ahmed, and Danai Koutra. Graph neural networks with heterophily. In *Proceedings of the AAAI Conference on Artificial Intelligence*, volume 35, pp. 11168–11176, 2021.

Jiong Zhu, Junchen Jin, Donald Loveland, Michael T Schaub, and Danai Koutra. How does heterophily impact the robustness of graph neural networks? theoretical connections and practical implications. In *Proceedings of the 28th ACM SIGKDD Conference on Knowledge Discovery and Data Mining*, pp. 2637–2647, 2022.

Appendices

This appendix is organized as follows. App. A presents more about HetFlows: Prerequisite knowledge of normalizing flows and affine coupling layers, training process, generation process, loss function, details of multi-channel message passing GNNs in HetFlows, computational issues and reversibility proof of the model. App. B illustrates related details of node classification experiment, including the experiment environment, data sets information and message passing details of GNNs used as base models. App. C provides the experiment environment, data sets, additional experiment results for molecule generation, property optimization algorithm with corresponding results together and model selection details. App. D summarizes and describes the metrics used in the molecular generation experiments.

A HetFlows Details

This section presents all the technical details of HetFlows.

A.1 Prerequisites: Normalizing Flows with Affine Coupling Layers

Affine coupling layers (ACLs) introduce reversible transformations to normalizing flows, ensuring efficient computation of the log-determinant of the Jacobian (Kingma & Dhariwal, 2018). Typically, the affine coupling layer, denoted by $\mathrm{ACL}^{(f,\boldsymbol{M})}$, contains a binary masking matrix $\boldsymbol{M} \in \{0,1\}^{m\times n}$ and a **coupling function** f which determines the affine transformation parameters. The input $\boldsymbol{X} \in \mathbb{R}^{m\times n}$ is split into $\boldsymbol{X}_1 = \boldsymbol{M} \odot \boldsymbol{X}$ and $\boldsymbol{X}_2 = (\mathbf{1} - \boldsymbol{M}) \odot \boldsymbol{X}$ by masking, where '$\odot$' denotes the Hadamard (element-wise) product. Here, $\boldsymbol{X}_1$ is the masked input that will undergo the transformation, and $\boldsymbol{X}_2$ is the part that provides parameters for this transformation via the coupling function and stays invariant inside the ACLs. The output is the concatenation of the transformed part and the fixed part, as visualized in Fig. A5 given as:

$$\mathrm{ACL}^{(f,\boldsymbol{M})}(\boldsymbol{X}) = \boldsymbol{M} \odot (\boldsymbol{S} \odot \boldsymbol{X}_1 + \boldsymbol{T}) + (\mathbf{1} - \boldsymbol{M}) \odot \boldsymbol{X}_2, \tag{9}$$

such that $\log \boldsymbol{S}, \boldsymbol{T} = f(\boldsymbol{X}_2)$. The binary masking ensures that only part of the input is transformed, allowing the model to update certain features while fixing others, enabling the model's reversibility. The coupling functions of flow capture intricate data characteristics, into which we incorporate heterophily priors.

Normalizing flows offers a methodological approach to model distribution based on the change-of-variable law of probabilities. This is achieved by applying a chain of reversible and bijective transformations between trivial variables (like Gaussian) with target data variables and updating the transformation to minimize the negative log-likelihood (Dinh et al., 2014). Given a target distribution $\boldsymbol{z}_0 \sim p_{\boldsymbol{z}}$, we initialize flows $f = f_T \circ \cdots \circ f_1$. The flow reach trivial varibales $\boldsymbol{z}_T \sim \mathrm{N}(\mu, \sigma^2)$ through a series of invertible functions: $\boldsymbol{z}_i = f_i(\boldsymbol{z}_{i-1}), i = 1, 2, \ldots, T$. The goal of normalizing flows is to minimize the negative log-likelihoods (NLLs) of the data:

$$\mathcal{L} = -\log p_{\boldsymbol{z}}(\boldsymbol{z}_0) = -\log \mathrm{N}(\boldsymbol{z}_T \mid \mu, \sigma^2) - \log \det \left| \frac{\partial f}{\partial \boldsymbol{z}_0} \right|. \tag{10}$$

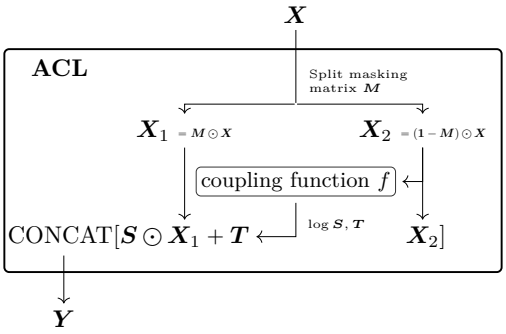

Figure A5: The affine coupling layer. The coupling is defined through a coupling function f and binary masking matrix $\boldsymbol{M}$ (seen in Eq. (9)).

The power of normalizing flows lies in their bijectiveness. This ensures that no information from the data is lost during these transformations. Thus, the transformed distribution can be 'pulled back' to the original space using the inverse of the transformation functions, providing a bridge between the Gaussian and the intricate target distribution.

A.2 Training Process

Molecule graph G contains atom (node) features $\boldsymbol{X} \in \mathbb{R}^{n \times n_a}$ and bond (edge) features $\boldsymbol{E} \in \mathbb{R}^{n \times n \times n_b}$. The terms n_a and n_b denote the types amount of atoms and bonds respectively. And $(\boldsymbol{X})_i$ denotes the one-hot encoded type of the ith atom present in molecule G. Similarly, $(\boldsymbol{E})_{ij}$ denotes the one-hot encoding of the specific chemical bond between the ith and j^{th} atoms. Our model HetFlows maps the molecule G to embeddings $\boldsymbol{h}_a$ and $\boldsymbol{h}_b$ that follow the Gaussian distributions:

$$\boldsymbol{h}_a \sim p_a = \mathrm{N}(\mu_a, \sigma_a^2), \quad \boldsymbol{h}_b \sim p_b = \mathrm{N}(\mu_b, \sigma_b^2). \tag{11}$$

Bond flow The bond flow represented by $f_b = \mathrm{ACL}_{k_b}^b \circ \cdots \circ \mathrm{ACL}_1^b$ consists of a series of ACLs with convolutional neural networks (CNNs) as coupling function: $\mathrm{ACL}_i^b = \mathrm{ACL}^{(\mathrm{CNN}_i, \boldsymbol{M}_i^b)}, \boldsymbol{M}_i^b \in \mathbb{R}^{n \times n \times n_b} \quad i = 1, 2, \ldots, k_b$, where k_b denotes the number of layers. Then bond embeddings $\boldsymbol{h}_b = \boldsymbol{h}_b^{(k_b)} = f_b(\boldsymbol{h}_b^{(0)})$ are updated by layers:

$$\boldsymbol{h}_b^{(i)} = \mathrm{ACL}_i^b \left(\boldsymbol{h}_b^{(i-1)} \right), \quad i = 1, 2, \ldots, k_b. \tag{12}$$

initialized from the bond tensor $\boldsymbol{h}_b^{(0)} = \boldsymbol{E}$

Heterophilous atom flow The atom flow f_a contains k_a affine coupling layers. Each layer consists of a masking matrix $\boldsymbol{M}$ and a GNN coupling function GNN^Γ.

$$\mathrm{ACL}_i^a = \mathrm{ACL}^{(\mathrm{GNN}_i^\Gamma, \boldsymbol{M}_i)}, \quad i = 1, 2, \ldots, k_a. \tag{13}$$

where $(\boldsymbol{M}_i)_{j,k} = \mathbf{1}_{j \equiv i(n)}$, and $\Gamma = \{\text{orig.}, \text{hom.}, \text{het.}\}$ indicate MP scheme as mentioned in Sec. 3.1. GNN^Γ is a multi-channel MP GNN combining these three schemes as described at App. A.5. All GNNs in this context derive their graph topology $(\mathcal{E}, \boldsymbol{E})$ from the bond tensor $\boldsymbol{E}$. The embeddings are initialized by the atom features: $\boldsymbol{h}_0^{(a)} = \boldsymbol{X}$, and undergo an update through each affine coupling layer as follows:

$$\boldsymbol{h}_a^{(i)} = \mathrm{ACL}_i^a \left(\boldsymbol{h}_a^{(i-1)} \mid \boldsymbol{E} \right), \quad i = 1, 2, \ldots, k_a. \tag{14}$$

The final node embedding is $\boldsymbol{h}_a = \boldsymbol{h}_a^{(k_a)} = f_a(\boldsymbol{h}_a^{(0)})$.

Training target The training goal of HetFlows is to decrese the distance between the transformed variables $\{\boldsymbol{h}_a, \boldsymbol{h}_b\}$ with target distribution p_a, p_b, as assumed in Eq. (11). The loss function combines the NLLs from both the atom and bond flow: $\mathcal{L} = \mathcal{L}_a + \mathcal{L}_b$ (details at App. A.4). Each NLL is given as shown in Eq. (10). The target of training is to search for model parameters to minimize the loss:

$$f_{a*}, f_{b*} = \underset{f_a, f_b}{\arg\min}\ \mathcal{L} \tag{15}$$

A.3 Generation Process

Given a trained HetFlows model, with established atom flow f_{a*} and bond flow f_{b*}, the procedure for generating molecules is described as follows ($*$ denotes parameters fixed).

1. **Sampling Embeddings:** Start by randomly sampling embeddings $\boldsymbol{h}_a \sim p_a$ and $\boldsymbol{h}_b \sim p_b$ from a Gaussian distribution as expressed in Eq. (11).

2. **Obtaining the Bond Tensor:** The bond tensor $\boldsymbol{E}$ can be derived by applying the inverse of the bond flow f_{b*}^{-1} to the sampled embedding $\boldsymbol{h}_b$. This is given as $\boldsymbol{E} = f_{b*}^{-1}(\boldsymbol{h}_b)$.

3. **Recovering Graph Topology:** From the bond tensor $\boldsymbol{E}$, the graph topology $(\mathcal{E}, \boldsymbol{E})$ can be deduced. This topology is essential for the node feature generation at the next step.

4. **Generating Node Features:** With the bond tensor in place, the generated node features can be produced by applying the inverse of the atom flow f_{a*}^{-1} to the sampled atom embedding $\boldsymbol{h}_a$ given by $\boldsymbol{X} = f_{a*}^{-1}(\boldsymbol{h}_a \mid \boldsymbol{E})$.

5. **Molecule Recovery:** Finally, a molecule, represented as $G = (\boldsymbol{X}, \boldsymbol{E})$, can be reconstructed from random embeddings $[\boldsymbol{h}_a, \boldsymbol{h}_b]$.

The topology generation process (Steps 2–3) can be achieved by sampling the adjacency matrix from the real (data) distribution.

Reversibility of HetFlows

To ensure that the molecular embeddings produced by HetFlows can be inverted back, it is crucial to understand the reversibility of the processes. A formal proof of reversibility of ACL blocks and HetFlows is provided in App. A.7.

A.4 Loss function

The loss function of the HetFlows is the NLLs of flows $\mathcal{L} = \mathcal{L}_a + \mathcal{L}_b$ consists of atom flows and bond flows. The details are listed as follows: The bond model loss $\mathcal{L}_a$ comes from the NLLs as the Eq. (10)

$$\mathcal{L}_b = -\log p\left(\boldsymbol{h}_b\right) - \sum_{i=1}^{k_b} \log\det\left(\left|\frac{\partial \mathrm{ACL}_i^b}{\partial \boldsymbol{h}_b^{(i-1)}}\right|\right). \tag{16}$$

Similarly, the loss $\mathcal{L}_a$ for the atom flow can be constructed as:

$$\mathcal{L}_a = -\log p\left(\boldsymbol{h}_a\right) - \sum_{i=1}^{k_a} \log\det\left(\left|\frac{\partial \mathrm{ACL}_i^a}{\partial \boldsymbol{h}_a^{(i-1)}}\right|\right). \tag{17}$$

A.5 The Multi-channel Message Passing Graph Neural Network

In the code implementation, the multi-channel MP GNN, GNN^{Γ} ($\Gamma = \{\mathrm{orig.}, \mathrm{hom.}, \mathrm{het.}\}$), consists of convolutional layers, batch normalization layers and a series of linear layers. The convolutional layer is the improved version of the graph convolutional layer of GCNs (Kipf & Welling, 2017), with three channels of MP. Each channel transfers messages between neighbours by certain preferences based on the homophily/heterophily.

Given input $\boldsymbol{h} \in \mathbb{R}^{n \times n_a}$ and bond tensor $\boldsymbol{E} \in \mathbb{R}^{n \times n \times n_b}$, assume the adjacency matrix $\boldsymbol{A}_i = \boldsymbol{E}[:,:,i] \in \mathbb{R}^{n \times n}$, $i = 1, \ldots, n_b$. Here n_a, n_b are the feature dimensions of node and bond. Then the messages are scaling with the scaling matrix $\boldsymbol{H}_\gamma \in \mathbb{R}^{n \times n}$, and $(\boldsymbol{H}_\gamma)_{ij} = \alpha_{ij,\gamma}$. The homophily factors $\alpha_{uv,\gamma}$ differ from channels indicated by $\gamma \in \Gamma$

$$\alpha_{uv,\gamma} = \begin{cases} \mathcal{H}(u,v), & \text{if } \gamma = \text{hom.} \\ 1, & \text{if } \gamma = \text{orig.} \\ 1 - \mathcal{H}(u,v), & \text{if } \gamma = \text{het.}, \end{cases} \tag{18}$$

and $\mathcal{H}(u,v) \triangleq S_{\cos}(\boldsymbol{h}_u^{(k)}, \boldsymbol{h}_v^{(k)})$ is the cosine similarity. The node embeddings are updated by the transferred messages in these triple channels, for each edge channel i,

$$\hat{\boldsymbol{h}}_i = \mathrm{cat}\left(\boldsymbol{H}_{\mathrm{orig.}} \odot \boldsymbol{A}_i \boldsymbol{h}, \boldsymbol{H}_{\mathrm{hom.}} \odot \boldsymbol{A}_i \boldsymbol{h}, \boldsymbol{H}_{\mathrm{het.}} \odot \boldsymbol{A}_i\right) \hat{\boldsymbol{W}}_i, \tag{19}$$

for $i = 1, \ldots, n_b$, where the $\{\boldsymbol{W}_i \in \mathbb{R}^{n_a \times n_{out}}\}_{i=1}^{n_b}$ are the model parameters, and cat denotes the concatenation operator, n_{out} is the expected output dimension. Then the output of this convolutional layer is the sum of all edge types

$$\hat{\boldsymbol{h}} = \sum_{i=1}^{n_b} \hat{\boldsymbol{h}}_i \ \in \mathbb{R}^{n \times n_{out}}. \tag{20}$$

In conclusion, given the input $\boldsymbol{h} \in \mathbb{R}^{n \times n_a}$ and bond tensor $\boldsymbol{E} \in \mathbb{R}^{n \times n \times n_b}$, the convolutional layer generates ouput

$$\mathrm{GNN}^{\Gamma}(\boldsymbol{h} \mid \boldsymbol{E}) = \hat{\boldsymbol{h}} \in \mathbb{R}^{n \times n_{out}}. \tag{21}$$

A.6 Computational Considerations

For convenience on the calculation of the log-likelihood, every transformation of variables needs the calculation of a Jacobian matrix (*i.e.*, $\partial \boldsymbol{Z}^{(l+1)} / \partial \boldsymbol{Z}^{(l)}$). So all the complicated modules (*e.g.*, GNNs, MLPs) are all built inside the coupling structure (part of the input is updated by the scaling matrix $\boldsymbol{S}$, and transformation matrix $\boldsymbol{T}$ depends on the other part of the input).

A.7 Proof of Reversibility of HetFlows

Both the atom and bond models of HetFlows rely on ACL blocks. As introduced in App. A.1, these blocks are inherently reversible. This means they can forward process the input to produce an output and can also take that output to revert it to the original input without loss of information. Besides the use of ACL blocks, the operations used within the model primarily leverage simple concatenation or permutation. These operations are straightforward and do not affect the overall reversibility of the processes. Given that the individual components (both atom and bond flows) are reversible and the operations performed on the data are straightforward, thus that HetFlows as a whole is reversible. The formal proof of the model's reversibility is provided as follows.

A.7.1 Reversibility of the ACL

Claim The affine coupling layer (ACL) defined at App. A.1, the atom model f_a and bond model f_b defined at App. A.2 are reversible. **Set up** Assume an ACL (Kingma & Dhariwal, 2018) defined in App. A.1 contains coupling function f and masking matrix $\boldsymbol{M} \in \{0,1\}^{m \times n}$. Given input $\boldsymbol{X} \in \mathbb{R}^{m \times n}$, the output $\boldsymbol{Y}$ is calculated as

$$\begin{aligned} \boldsymbol{Y} &= \mathrm{ACL}^{(f,\boldsymbol{M})}(\boldsymbol{X}) \\ &= \boldsymbol{M} \odot (\boldsymbol{S} \odot \boldsymbol{X}_1 + \boldsymbol{T}) + (\boldsymbol{1} - \boldsymbol{M})\boldsymbol{X}_2 \end{aligned} \tag{22}$$

where $\log \boldsymbol{S}, \boldsymbol{T} = f(\boldsymbol{X}_2)$, and $\boldsymbol{X}_1, \boldsymbol{X}_2$ are the split from input by masking:

$$\boldsymbol{X}_1 = \boldsymbol{M} \odot \boldsymbol{X}, \quad \boldsymbol{X}_2 = (\boldsymbol{1} - \boldsymbol{M}) \odot \boldsymbol{X}. \tag{23}$$

We seek to recover $\boldsymbol{X}$ from the $f, \boldsymbol{M}$, and $\boldsymbol{Y}$.

Reversibility from output to input Since $\boldsymbol{M}$ is binary, we can get the following results .

$$\boldsymbol{M} \odot \boldsymbol{M} = \boldsymbol{M}, \tag{24}$$

$$(\boldsymbol{1} - \boldsymbol{M}) \odot (\boldsymbol{1} - \boldsymbol{M}) = (\boldsymbol{1} - \boldsymbol{M}), \tag{25}$$

$$\boldsymbol{M} \odot (\boldsymbol{1} - \boldsymbol{M}) = (\boldsymbol{1} - \boldsymbol{M}) \odot \boldsymbol{M} = \boldsymbol{0} \tag{26}$$

and

$$\boldsymbol{X} = (\boldsymbol{M} + (\boldsymbol{1} - \boldsymbol{M})) \odot \boldsymbol{X} \tag{27}$$

$$= \boldsymbol{M} \odot \boldsymbol{X} + (\boldsymbol{1} - \boldsymbol{M}) \odot \boldsymbol{X} \tag{28}$$

$$= \boldsymbol{X}_1 + \boldsymbol{X}_2. \tag{29}$$

By splitting the output $\boldsymbol{Y}$ to $\boldsymbol{Y}_1, \boldsymbol{Y}_2$ by masking matrix:

$$\boldsymbol{Y}_1 = \boldsymbol{M} \odot \boldsymbol{Y}, \quad \boldsymbol{Y}_2 = (\boldsymbol{1} - \boldsymbol{M}) \odot \boldsymbol{Y}. \tag{30}$$

Combining with Eq. (22), we know

$$\begin{aligned}
\boldsymbol{Y}_1 &= \boldsymbol{M} \odot \boldsymbol{Y} && (31)\\
&= \boldsymbol{M} \odot (\boldsymbol{M} \odot (\boldsymbol{S} \odot \boldsymbol{X}_1 + \boldsymbol{T}) + (\boldsymbol{1} - \boldsymbol{M}) \odot \boldsymbol{X}_2) && (32)\\
&= \boldsymbol{M} \odot (\boldsymbol{S} \odot \boldsymbol{X}_1 + \boldsymbol{T}), && (33)
\end{aligned}$$

and

$$\begin{aligned}
\boldsymbol{Y}_2 &= (\boldsymbol{1} - \boldsymbol{M}) \odot \boldsymbol{Y} && (34)\\
&= (\boldsymbol{1} - \boldsymbol{M}) \odot (\boldsymbol{M} \odot (\boldsymbol{S} \odot \boldsymbol{X}_1 + \boldsymbol{T}) \\
&\qquad + (\boldsymbol{1} - \boldsymbol{M}) \odot \boldsymbol{X}_2) && (35)\\
&= (\boldsymbol{1} - \boldsymbol{M}) \odot (\boldsymbol{M} \odot (\boldsymbol{S} \odot \boldsymbol{X}_1 + \boldsymbol{T}) \\
&\qquad + (\boldsymbol{1} - \boldsymbol{M}) \odot (\boldsymbol{1} - \boldsymbol{M}) \odot \boldsymbol{X}) && (36)\\
&= (\boldsymbol{1} - \boldsymbol{M}) \odot \boldsymbol{X} = \boldsymbol{X}_2. && (37)
\end{aligned}$$

Now the $\log \boldsymbol{S}, \boldsymbol{T} = f(\boldsymbol{X}_2) = \boldsymbol{Y}_2$ are recovered by $\boldsymbol{Y}$. Notice that

$$\begin{aligned}
&\boldsymbol{M} \odot (\boldsymbol{Y}_1 - \boldsymbol{T}) \oplus \boldsymbol{S} && (38)\\
&= \boldsymbol{M} \odot (\boldsymbol{M} \odot (\boldsymbol{S} \odot \boldsymbol{X}_1 + \boldsymbol{T}) - \boldsymbol{T}) \oplus \boldsymbol{S} && (39)\\
&= (\boldsymbol{M} \odot \boldsymbol{S} \odot \boldsymbol{X}_1 + \boldsymbol{M} \odot \boldsymbol{T} - \boldsymbol{M} \odot \boldsymbol{T}) \oplus \boldsymbol{S} && (40)\\
&= (\boldsymbol{M} \odot \boldsymbol{S} \odot \boldsymbol{X}_1) \oplus \boldsymbol{S} && (41)\\
&= \boldsymbol{M} \odot \boldsymbol{X}_1 && (42)\\
&= \boldsymbol{M} \odot \boldsymbol{M} \odot \boldsymbol{X} && (43)\\
&= \boldsymbol{M} \odot \boldsymbol{X} && (44)\\
&= \boldsymbol{X}_1 \quad \text{if} \quad (\boldsymbol{S})_{i,j} > 0, \quad \forall i, j, && (45)
\end{aligned}$$

where '$\oplus$' denotes element-wise division. Since we define $\boldsymbol{S}$ as the exponential part of the output from the coupling function, the elements of $\boldsymbol{S}$ are all strictly positive. Then

$$\begin{aligned}
\boldsymbol{X} &= \left(\mathrm{ACL}^{(f,\boldsymbol{M})}\right)^{-1}(\boldsymbol{Y}) \\
&= \boldsymbol{X}_1 + \boldsymbol{X}_2 \\
&= \boldsymbol{M} \odot (\boldsymbol{Y}_1 - \boldsymbol{T}) \oplus \boldsymbol{S} + \boldsymbol{Y}_2 \\
&= \boldsymbol{M} \odot (\boldsymbol{M} \odot \boldsymbol{Y} - \boldsymbol{T}) \oplus \boldsymbol{S} + (\boldsymbol{1} - \boldsymbol{M}) \odot \boldsymbol{Y}.
\end{aligned} \tag{46}$$

where $\log \boldsymbol{S}, \boldsymbol{T} = f(\boldsymbol{X}_2) = f((\boldsymbol{1} - \boldsymbol{M}) \odot \boldsymbol{Y}))$. Eq. (46) shows how the input is recovered from the output, thus the ACL block is reversible.

A.7.2 Reversibility of the Bond Model

For the bond model $f_b = \mathrm{ACL}^b_{k_b} \circ \cdots \circ \mathrm{ACL}^b_1$, and since each $\mathrm{ACL}^b_i,\ i = 1, \ldots, k_b$ is reversible, we can write $f_b^{-1} = \left(\mathrm{ACL}^b_1\right)^{-1} \circ \cdots \circ \left(\mathrm{ACL}^b_{k_b}\right)^{-1}$, which the reverse function of f_b.

A.7.3 Reversibility of the Atom Model

For the atom model $f_a = \mathrm{ACL}^a_{k_a} \circ \cdots \circ \mathrm{ACL}^a_1$, and since each $\mathrm{ACL}^a_i,\ i = 1, \ldots, k_a$ is reversible, we can write $f_a^{-1} = (\mathrm{ACL}^a_1)^{-1} \circ \cdots \circ \left(\mathrm{ACL}^a_{k_a}\right)^{-1}$, which the reverse function of f_a.

B Experiment Details: Node Classification

B.1 Hardware

All models in this experiment are trained on a Linux cluster equipped with NVIDIA V100 GPUs. The training time and memory requirement for single models were (for all modes orig., hom., or het. and for all base models):

- Texas: 5 mins, 2 GB
- Cornell: 5 mins, 2 GB
- Wisconsin: 5 mins, 2 GB
- Actor: 5 mins, 4 GB
- Squirrel: 10 mins, 16 GB
- Chameleon 5 mins, 4 GB
- CiteSeer: 5 mins, 2 GB
- Computers: 10 mins, 16 GB
- PubMed: 5 mins, 2 GB
- Cora: 5 mins, 2 GB
- CoauthorCS: 10 mins, 32 GB
- Photo: 5 mins, 8 GB

B.2 Data Sets

There are 12 data sets selected to conduct comprehensive and discriminative node classification tasks. To examine patterns associated with varying levels of data homophily, half of the data sets are chosen higher homophily, while the other half are more heterophilic. The data domains include citation networks (Yang et al., 2016) (Cora, PubMed, CiteSeer), co-purchase graphs (Shchur et al., 2018) (Computers, Photo), co-author network (Shchur et al., 2018) (CoauthorCS), hyperlink networks (Pei et al., 2019) (Cornell, Wisconsin, Texas), Wikipedia networks (Rozemberczki et al., 2021) (Chameleon, Squirrel), and actor co-occurrence network (Tang et al., 2009) (Actor).

Statistical information The descriptive statistics on all the data sets for node classification tasks in Sec. 4.1 are displayed in Table A4. Here, $N_{\text{graphs}}, N_{\text{nodes}}$ and N_{edges} denote the total amounts of graphs, nodes and edges in the data set respectively. $D_{\text{feat}}, N_{\text{class}}$ denote the dimensions of the node features and labels. $\mathcal{H}_n$ and $\mathcal{H}_e$ denote the average node homophily (Pei et al., 2019) and average edge homophily (Zhu et al., 2020) of the data set.

Data split rule For 6 heterophilic data sets (Cornell, Wisconsin, Texas, Actor, Chameleon, Squirrel), the data is split to train/validate/test with fixed 10 seeds from GEOM-GCN (Pei et al., 2019). For other datasets, the splitting is randomly controlled by the python *torch* package.

Each result contains 100 random runs (For each data split seed, 10 different random model initializations are applied).

B.3 GNN Algorithm Details

There are four classic GNNs utilized as base models in the node classification task of Sec. 4.1. Here we provide these algorithms by showing the message-passing details of a single convolutional layer.

Graph Convolutional Networks (GCN) The most classic graph convolutional operator is proposed by Kipf & Welling (2017). Given the embeddings $\boldsymbol{h}_v^{(k)}$ of node $v \in \mathcal{V}$ at k^{th} layer, the message for node u from node v is defined as

$$\boldsymbol{m}_{uv}^{(k)} = \frac{e_{u,v}}{(\hat{d}_u \hat{d}_v)^{1/2}} \boldsymbol{h}_v^{(k)}, \tag{47}$$

where $e_{u,v}$ denotes the weight of edge (u, v), $\hat{d}_v = 1 + \sum_{u \in \mathcal{N}(v)} e_{u,v}$ denotes the weighted degree of node v with self-loop. Then the node embeddings are updated by the message set $\{\{\boldsymbol{m}_{uv} | v \in \mathcal{N}(u) \cup \{u\}\}\}$ collected from all its neighbours

$$\boldsymbol{h}_u^{(k+1)} = \Theta^\top \sum_{u \in \mathcal{N}(u) \cup \{u\}} \boldsymbol{m}_{uv}^{(k)}, \tag{48}$$

where Θ denotes the model parameters.

Graph Attention Networks (GAT) Veličković et al. (2018) proposed the graph attention operator inspired by the transformer. Given the embeddings $\boldsymbol{h}_v^{(k)}$ of node $v \in \mathcal{V}$ at k^{th} layer, the message for node v from node u is defined as

$$\boldsymbol{m}_{uv}^{(k)} = \begin{cases} \alpha_{u,v} \Theta_t \boldsymbol{h}_u^{(k)} & \text{if } u \neq v \\ \alpha_{u,v} \Theta_s \boldsymbol{h}_v^{(k)} & \text{if } u = v \end{cases}, \tag{49}$$

where Θ_s, Θ_t denotes the model parameters, and $\alpha_{u,v}$ denotes the attention value from node v to node u

$$\alpha_{u,v} = \frac{\exp\left(\text{LR}(\boldsymbol{a}_s^\top \Theta_s \boldsymbol{h}_u + \boldsymbol{a}_t^\top \Theta_t \boldsymbol{h}_v)\right)}{\sum\limits_{w \in \mathcal{N}(u) \cup \{u\}} \exp\left(\text{LR}(\boldsymbol{a}_s^\top \Theta_s \boldsymbol{h}_u + \boldsymbol{a}_t^\top \Theta_t \boldsymbol{h}_w)\right)}. \tag{50}$$

where LR denotes the Leaky Rectified Linear Unit. Then the node embeddings are updated by the neighbour message set

$$\boldsymbol{h}_u^{(k+1)} = \sum_{u \in \mathcal{N}(u) \cup \{u\}} \boldsymbol{m}_{uv}^{(k)}. \tag{51}$$

Graph Isomorphism Network (GIN) The graph isomorphism operator is created by Xu et al. (2019) based on Weisfeiler-Lehman (WL) graph isomorphism test (Leman & Weisfeiler, 1968). Given the embeddings

Table A4: The statistic information on the data sets for node classification experiment in Sec. 4.1

	N_{graphs}	N_{nodes}	N_{edges}	D_{feat}	N_{class}	$\mathcal{H}_n$	$\mathcal{H}_e$
Texas	1	183	325	1703	5	0.104	0.108
Cornell	1	183	298	1703	5	0.106	0.131
Wisconsin	1	251	515	1703	5	0.134	0.196
Actor	1	7600	30019	932	5	0.205	0.219
Squirrel	1	5201	217073	2089	5	0.219	0.224
Chameleon	1	2277	36101	2325	5	0.249	0.235
CiteSeer	1	3327	9104	3703	6	0.706	0.736
Computers	1	13752	491722	767	10	0.785	0.777
PubMed	1	19717	88648	500	3	0.792	0.802
Cora	1	2708	10556	1433	7	0.825	0.810
CoauthorCS	1	18333	163788	6805	15	0.832	0.808
Photo	1	7650	238162	745	8	0.836	0.827

$\boldsymbol{h}_v^{(k)}$ of node $v \in \mathcal{V}$ at k^{th} layer, the message for node v from node u is the node embedding itself

$$\boldsymbol{m}_{uv}^{(k)} = \begin{cases} \boldsymbol{h}_v^{(k)} & \text{if } u \neq v \\ (1+\varepsilon)\boldsymbol{h}_u^{(k)} & \text{if } u = v \end{cases}, \tag{52}$$

where the ε controls the self-weight. Then the node embeddings are updated by the neighbour message set through another neural network h_θ

$$\boldsymbol{h}_u^{(k+1)} = h_\theta \left(\sum_{u \in \mathcal{N}(u) \cup \{u\}} \boldsymbol{m}_{uv}^{(k)} \right). \tag{53}$$

The h_θ is often defined as a simple MLP.

GraphSAGE Hamilton et al. (2017) highlights the sample and aggregation approach in their GraphSAGE operator. Given the embeddings $\boldsymbol{h}_v^{(k)}$ of node $v \in \mathcal{V}$ at k^{th} layer, the message for node v from node u is the node embedding itself

$$\boldsymbol{m}_{uv}^{(k)} = v h_v^{(k)} u, \tag{54}$$

Then the node embeddings are updated as

$$\boldsymbol{h}_u^{(k+1)} = \Theta_1 \boldsymbol{m}_{uu} + \Theta_2 \frac{1}{|\mathcal{N}(u)|} \sum_{v \in \mathcal{N}(u)} \boldsymbol{m}_{uv}, \tag{55}$$

where Θ_1, Θ_2 are the model parameters.

C Experiment Details: Molecule Generation

C.1 Hardware

All models in this experiment are trained on a cluster equipped with NVIDIA A100 GPUs. The training time for a single model was 10 h (QM9) and 90 h (ZINC-250K).

The training time and memory requirement for single models were (for all modes orig., hom.or het.and for all base models)

- QM9: 10 h, 8 GB
- ZINC-250K: 90 h, 16 GB

C.2 Data sets

Two classic molecule data sets (QM9 and ZINC-250K), which are widely used in academia, are chosen for the molecular generation task. The QM9 data set (Ramakrishnan et al., 2014) comprises ∼134k stable small organic molecules composed of atoms from the set {C, H, O, N, F}. The ZINC-250K (Irwin et al., 2012) data contains ∼250k drug-like molecules, each with up to 38 atoms of 9 different types.

Data split In this experiment, all data sets are split with ratio train/test = 80/20%.

C.3 Further Results

Latent-space exploration We provide further results for structured latent-space exploration. Example explorations for QM9 and ZINC-250K are shown in Fig. 4 and Fig. A6.

Overall 14 metrics tables We include full listings of all 14 metrics (description of metrics in App. D) considered in the random generation tasks for QM9 and ZINC-250K. The values are listed in Tables A5 and A6, respectively.

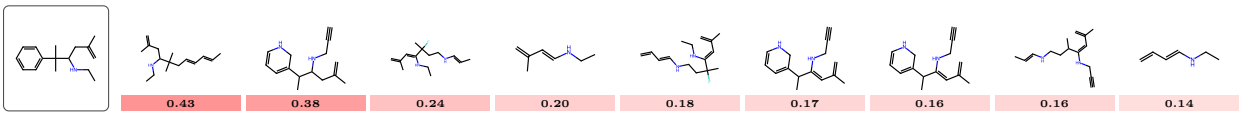

Figure A6: **Structured latent-space exploration (ZINC-250K).** Example of nearest neighbour search in the latent space with the seed molecules on the left and neighbours with the Tanimoto similarity (1 0) given for each molecule. For results on QM9, see Fig. 4 in the main paper.

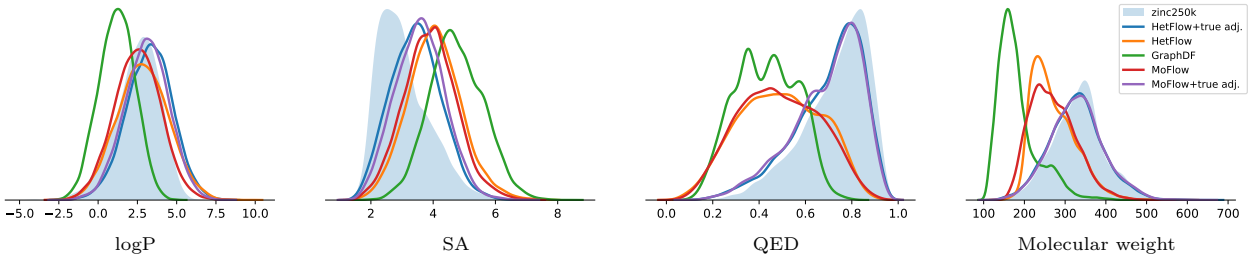

Figure A7: Chemoinformatics statistics for data (ZINC-250K) and generated molecules from HetFlows (ours), MoFlow, and GraphDF. Histograms for the Octanol-water partition coefficient (logP), synthetic accessibility score (SA), quantitative estimation of drug-likeness (QED), and molecular weight.

Table A5: Full benchmark metrics for random generation using QM9 (reporting mean±std)

		Validity ↑	Uniqueness ↑	Novelty ↑	SNN ↑	Frag ↑	Scaf ↑	IntDiv_1 ↑
	Data (QM9)	1.00±0.00	1.00±0.00	0.62±0.02	0.54±0.00	0.94±0.01	0.76±0.03	0.92±0.00
Flows	GraphDF	-	**1.00**±0.00	**0.98**±0.00	0.35±0.00	0.61±0.01	0.09±0.07	0.87±0.00
	MoFlow	0.95±0.01	**1.00**±0.00	0.96±0.01	0.32±0.00	0.60±0.03	0.04±0.03	**0.92**±0.00
	HetFlow (Ours)	0.92±0.01	0.99±0.00	0.92±0.01	0.34±0.00	0.80±0.02	0.04±0.03	0.91±0.00
Abl.	MoFlow+true adj.	**1.00**±0.00	**1.00**±0.00	0.85±0.01	0.38±0.00	0.70±0.03	0.31±0.08	**0.92**±0.00
	HetFlow+true adj.	**1.00**±0.00	**1.00**±0.00	0.74±0.01	0.43±0.00	0.85±0.02	0.52±0.05	**0.92**±0.00
Diff.	EDM	0.92±0.01	**1.00**±0.00	0.56±0.02	**0.48**±0.01	**0.92**±0.01	**0.65**±0.03	**0.92**±0.00

		IntDiv_2 ↑	Filters ↑	FCD ↓	ΔlogP ↓	ΔSA ↓	ΔQED ↓	ΔWeight ↓
	Data (QM9)	0.90±0.00	0.64±0.02	0.40±0.02	0.04±0.01	0.03±0.01	0.00±0.00	0.32±0.08
Flows	GraphDF	0.86±0.00	**0.69**±0.02	10.76±0.21	0.16±0.03	0.27±0.02	0.05±0.00	19.72±0.54
	MoFlow	**0.90**±0.00	0.55±0.02	7.55±0.23	0.40±0.02	0.41±0.02	0.04±0.00	3.75±0.08
	HetFlow (Ours)	**0.90**±0.00	0.62±0.02	4.04±0.24	**0.11**±0.02	0.34±0.01	0.03±0.00	4.40±0.11
Abl.	MoFlow+true adj.	**0.90**±0.00	0.60±0.01	4.45±0.11	0.65±0.02	0.56±0.02	0.04±0.00	**0.74**±0.14
	HetFlow+true adj.	**0.90**±0.00	0.62±0.01	1.46±0.09	0.26±0.02	0.36±0.02	0.02±0.00	1.12±0.18
Diff.	EDM	**0.90**±0.00	0.61±0.01	**0.96**±0.08	0.16±0.04	**0.15**±0.04	**0.01**±0.00	1.87±0.16

The reconstruction example For better understanding, we provide reconstruction examples on QM9 from intermediate layers in Fig. A8.

Homophily distribution of generated molecules Additionally, we also visualize the node homophily (in the 'neighbour-counting' sense as in **??**) for both QM9 and ZINC-250K together with the estimated node homophily histograms (see Fig. A9) from the generation outputs from the different models. The adjacency matrix generation strategies have a minor influence on the homophily distribution of generated molecules, it shows these statistics mostly rely on the atom model but not the bond model.

Ablation study The random generation of HetFlows with/without parameters sharing in the Multi-channel MP GNNs are shown in Table A7 and Table A8

Table A6: Full benchmark metrics for random generation using ZINC-250K (reporting mean±std)

		Validity ↑	Uniqueness ↑	Novelty ↑	SNN ↑	Frag ↑	Scaf ↑	IntDiv_1 ↑
	Data (ZINC-250K)	1.00±0.00	1.00±0.00	0.02±0.00	0.51±0.00	1.00±0.00	0.28±0.02	0.87±0.00
Flows	GraphDF	-	**1.00**±0.00	**1.00**±0.00	0.23±0.00	0.35±0.01	0.00±0.00	**0.88**±0.00
	MoFlow	0.89±0.01	**1.00**±0.00	**1.00**±0.00	0.27±0.00	0.79±0.01	0.01±0.00	**0.88**±0.00
	HetFlow (Ours)	0.87±0.01	**1.00**±0.00	**1.00**±0.00	0.26±0.00	0.77±0.01	0.01±0.00	**0.88**±0.00
Abl.	MoFlow+true adj.	**0.94**±0.01	**1.00**±0.00	**1.00**±0.00	0.33±0.00	0.89±0.01	0.07±0.02	0.87±0.00
	HetFlow+true adj.	0.93±0.01	**1.00**±0.00	**1.00**±0.00	**0.34**±0.00	**0.91**±0.01	**0.10**±0.03	0.87±0.00

		IntDiv_2 ↑	Filters ↑	FCD ↓	ΔlogP ↓	ΔSA ↓	ΔQED ↓	ΔWeight ↓
	Data (ZINC-250K)	0.86±0.00	0.59±0.01	1.44±0.01	0.05±0.01	0.03±0.01	0.01±0.00	2.18±0.39
Flows	GraphDF	**0.87**±0.00	0.54±0.01	34.30±0.30	1.28±0.03	1.70±0.03	0.30±0.00	149.27±1.55
	MoFlow	0.86±0.00	0.51±0.02	23.33±0.35	**0.15**±0.02	0.82±0.03	0.25±0.01	56.71±2.64
	HetFlow (Ours)	**0.87**±0.00	0.51±0.01	23.72±0.19	0.50±0.04	0.99±0.03	0.25±0.01	51.90±1.65
Abl.	MoFlow+true adj.	0.86±0.00	0.67±0.02	**8.21**±0.22	0.64±0.04	0.54±0.03	**0.04**±0.00	**4.23**±0.51
	HetFlow+true adj.	0.86±0.00	**0.75**±0.01	8.24±0.17	0.82±0.04	**0.41**±0.03	**0.04**±0.00	5.05±0.77

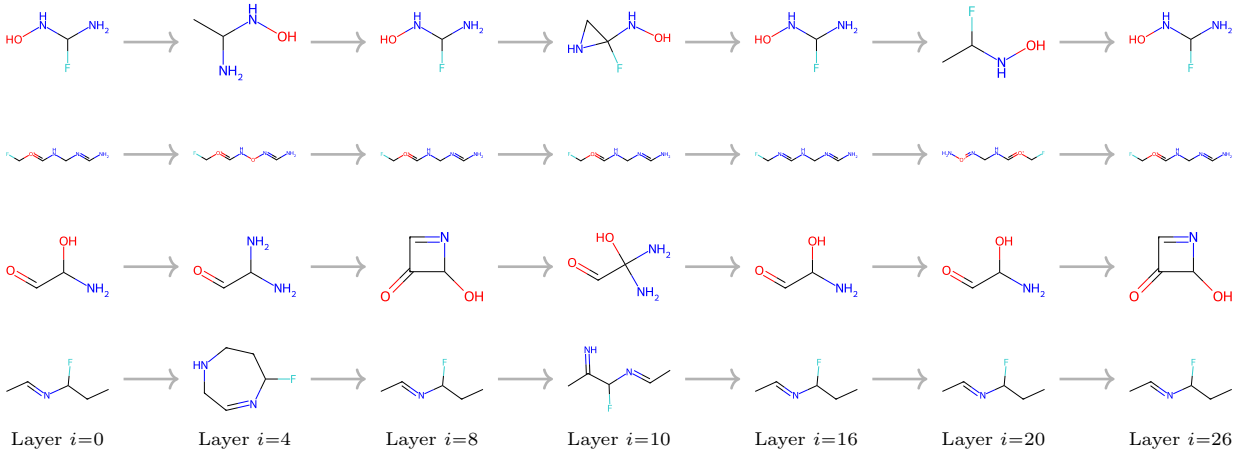

Figure A8: **Step-by-step generation (QM9).** Snapshots of reconstructed molecules when fixing the bond model and collecting node embeddings of the intermediate layers i.

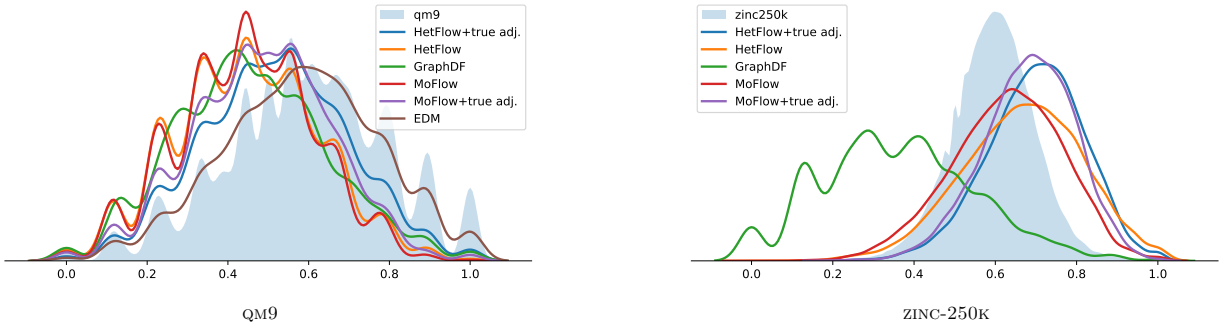

Figure A9: Node homophily distribution of generated molecules.

C.4 Property Optimization

In the property optimization task, models show their capability to find novel molecules that optimize specific chemical properties not present in the training data set: a critical component for drug discovery. For our

Table A7: Ablation study of heterophilous GNN parameter sharing on QM9

	FCD ↓	Validity ↑	Novelty ↑	SNN ↑	Frag ↑	Scaf ↑	IntDiv_1 ↑
Data (QM9)	0.40±0.02	1.00±0.00	0.62±0.02	0.54±0.00	0.94±0.01	0.76±0.03	0.92±0.00
HetFlow+true adj.	**1.46**±0.09	**1.00**±0.00	0.74±0.01	**0.43**±0.00	0.85±0.02	**0.52**±0.05	**0.92**±0.00
HetFlow+true adj.+share para.	1.66±0.07	**1.00**±0.00	**0.77**±0.01	0.42±0.00	**0.86**±0.02	0.48±0.05	**0.92**±0.00

Table A8: Ablation study of heterophilous GNN parameter sharing on ZINC-250K

	FCD ↓	Validity ↑	Novelty ↑	SNN ↑	Frag ↑	Scaf ↑	IntDiv_1 ↑
Data (ZINC-250K)	1.44±0.01	1.00±0.00	0.02±0.00	0.51±0.00	1.00±0.00	0.28±0.02	0.87±0.00
HetFlow+true adj.	8.24±0.17	**0.93**±0.01	**1.00**±0.00	**0.34**±0.00	0.91±0.01	**0.10**±0.03	**0.87**±0.00
HetFlow+true adj.+share para.	**8.11**±0.21	**0.93**±0.01	**1.00**±0.00	0.32±0.00	**0.93**±0.01	0.05±0.02	**0.87**±0.00

Table A9: Performance on molecule property optimization in terms of the best QED scores, scores taken from the corresponding papers (JTVAE score from Luo et al., 2021; Verma et al., 2022).

Method	1st	2nd	3rd
Data (ZINC-250K)	0.948	0.948	0.948
JTVAE	0.925	0.911	0.910
GCPN	**0.948**	0.947	0.946
GraphAF	**0.948**	**0.948**	0.947
GraphDF	**0.948**	**0.948**	**0.948**
MoFlow	**0.948**	**0.948**	**0.948**
ModFlow	**0.948**	**0.948**	0.945
HetFlows	**0.948**	**0.948**	0.947

study, we focused on maximizing the QED property. We trained HetFlows on ZINC-250K and evaluated its performance against other state-of-the-art models (Verma et al., 2022; Luo et al., 2021; Zang & Wang, 2020; Shi et al., 2019; Jin et al., 2018; You et al., 2018). The results, given in Table A9, show that the top three novel molecule candidates identified by HetFlows (not part of the ZINC-250K data set), exhibit QED values on par with those from ZINC-250K or other state-of-the-art methods.

Algorithm Given a pre-trained HetFlows f, and training set $\mathcal{D}$ contains molecule and property label pairs $\{G, y\}$. Now we introduce an extra simple MLP g_θ, which maps the molecular embeddings $f(G)$ into the predicted property

$$y_p = g_\theta(f(G)), \tag{56}$$

it is trained on the dataset to be $g_{\theta*}$ by optimizing the parameters:

$$\theta^* = \arg\min_\theta \underset{(G,y)\in\mathcal{D}}{\text{MSEloss}}(g_\theta(f(G)), y) \tag{57}$$

Then we find molecule candidates $\{G_i\}_{i=1}^k$ with top-k properties in the data set $\mathcal{D}$ are chosen. New embeddings are explored by optimizing the predict label by $g_{\theta*}$ starting from these candidates:

$$\begin{aligned} \boldsymbol{h}_{i,j} &= \delta \frac{\partial g_{\theta*}}{\partial \boldsymbol{h}}(\boldsymbol{h}_{i,j-1}) + \boldsymbol{h}_{i,j-1}, \quad j = 1, \ldots, N, \\ \boldsymbol{h}_{i,0} &= f(G_i), \quad i = 1, \ldots, k, \end{aligned} \tag{58}$$

where δ denotes the search step length, and N is the number of iterations. These embeddings could be recovered to be molecule set:

$$\mathcal{D}' = \{f^{-1}(\boldsymbol{h}_{ij})\}_{i=1,\ldots,k, \quad j=1,\ldots,N}. \tag{59}$$

Finally, $\mathcal{D}'\backslash\mathcal{D}$ gives the novel molecule sets with related high target properties.

Generation results In our experiments, the g_θ is a simple 3-layer MLP with 16 hidden nodes, the dataset $\mathcal{D}$ is ZINC-250K, and target property y is QED. And $\mathcal{D}'\backslash\mathcal{D}$ provides 17 molecules with QED score 0.948. The Top-3 QED score and molecular SMILES are listed below:

1. Cc1cc(C(=O)NC2CC2)c(C)n1-c1ccc2c(c1)OCCO2.N, QED = 0.947936,
2. Cc1cccnc1NC(=O)C1CC(=O)N(C)C1c1ccccc1, QED = 0.947505,
3. Cc1nn(C)c(C)c1C(=O)NCC1CC12CCc1ccccc12, QED = 0.947317.

Baselines The baselines scores of GCPN (You et al., 2018), GraphAF (Shi et al., 2019), GraphDF (Luo et al., 2021), MoFlow (Zang & Wang, 2020) and ModFlow (Verma et al., 2022) are acquired from the corresponding papers. The score of JTVAE (Jin et al., 2018) is acquired from Zang & Wang (2020); Verma et al. (2022).

C.5 Model selection

The ranges of HetFlows hyperparameters are listed as follows:

- The residual connection of ACL coupling function: [True, False]
- The parameter sharing mode of $\ln \mu_a, \ln \mu_b$: $[0, 1, 2]$. Here μ_a, μ_b are the variance of the embeddings distribution $\mathcal{N}_a, \mathcal{N}_b$ in Eq. (7).
  - mode 0 means the distribution variance of both node and edge embeddings are fixed to be 1: $\ln \mu_a = \ln \mu_b = 0$.
  - mode 1 means the distribution variance of both node and edge embeddings share one parameter: $\ln \mu_a = \ln \mu_b$, it could be optimized during the training process.
  - mode 2 means the distribution variance of both node and edge embeddings are separate parameters: $\ln \mu_a, \ln \mu_b$, both of them could be optimized the during training process.

The best-performing model is selected using the FCD score as suggested in Polykovskiy et al. (2020).

The HetFlows reported in the paper is selected with hyperparameters:

- The residual connection of ACL coupling function: False
- The parameter sharing mode of $\ln \mu_a, \ln \mu_b$: 1.

D Description of Chemoinformatics Metrics

For benchmarking, model selection, comparison, and explorative analysis, we use the following 14 metrics. The metrics are presented in detail in the work by Polykovskiy et al. (2020) that introduced the MOSES benchmarking platform. The metrics calculation makes heavy use of the RDKit open-source cheminformatics software (`https://www.rdkit.org/`). We briefly summarize the metrics below.

Sanity check metrics

1. **Validity** Fraction (in $[0, 1]$) of the molecules that produce valid SMILES representations. This is a sanity check for how well the model captures explicit chemical constraints such as proper valence. Higher values are better as a low value can indicate that the model does not properly capture chemical structure. We report numbers without *post hoc* validity corrections.
2. **Uniqueness** Fraction (in $[0, 1]$) of the molecules that are unique. This is a sanity check based on the SMILES string representation of the generated molecules. Higher values are better as a low value can indicate the model has collapsed and produces only a few typical molecules.
3. **Novelty** Fraction (in $[0, 1]$) of the generated molecules that are not present in the training set. Higher values are better as a low value can indicate overfitting to the training data set.

Summary statistics

4. **Similarity to a nearest neighbour (SNN)** The average Tanimoto similarity (Jaccard coefficient) in $[0, 1]$ between the generated molecules and their nearest neighbour in the reference data set. Higher is better: If the generated molecules are far from the reference set, similarity to the nearest neighbour will be low.

5. **Fragment similarity (Frag)** Measures similarity (in $[0, 1]$) of distributions of BRICS fragments (substructures) in the generated set vs. the original data set. If molecules in the two sets share many of the same fragments in similar proportions, the Frag metric will be close to 1 (higher better).

6. **Scaffold similarity (Scaf)** Measures similarity (in $[0, 1]$) of distributions of Bemis–Murcko scaffolds (molecule ring structures, linker fragments, and carbonyl groups) in the generated set vs. the original data set. This metric is calculated similarly to the Fragment similarity metric by counting substructure presence in the data, and they can be high even if the data sets do not contain the same molecules.

7. **Internal diversity ($\mathbf{IntDiv_1}$)** Measure (in $[0, 1]$) of the chemical diversity within the generated set of molecules. Higher values are better and signal higher diversity in the generated set of molecules. Low values can signal mode collapse.

8. **Internal diversity ($\mathbf{IntDiv_2}$)** Measure (in $[0, 1]$) of the chemical diversity within the generated set of molecules. The interpretation is similar to IntDiv_1 but with stronger penalization of the Tanimoto similarity in calculating the diversity.

9. **Filters** This metric is specific to the MOSES benchmarking platrofm (see Polykovskiy et al., 2020). It gives the fraction (in $[0, 1]$) of generated molecules that pass filters applied during data set construction. In practice, these filters may filter out chemically valid molecules with fragments that are not of interest in the MOSES data set (filtered with medicinal chemistry filters). Thus, this metric is not of primary interest to us but gives a view on the match with the MOSES data set.

10. **Fréchet ChemNet distance (FCD)** Analogous to the Frechét Inception Distance (FID) used in image generation, FCD compares feature distributions of real and generated molecules using a pre-trained model (ChemNet). Lower values are better.

Descriptive distributions

11. **Octanol-water partition coefficient (logP)** A logarithmic measure of the relationship between lipophilicity (fat solubility) and hydrophilicity (water solubility) of a set of molecules. For large values a substance is more soluble in fat-like solvents such as n-octanol, and for small values more soluble in water. We report both histograms of logP and a summary statistic in terms of the Wasserstein distance between the generated and reference distributions (smaller better).

12. **Synthetic accessibility score (SA)** A metric that estimates how easily a chemical molecule can be synthesized. It provides a quantitative value indicating the relative difficulty or ease of synthesizing a molecule, with a lower SA score suggesting that a molecule is more easily synthesized, and a higher score suggesting greater complexity or difficulty. We report both histograms of SA and a summary statistic in terms of the Wasserstein distance between the generated and reference distributions (smaller better).

13. **Quantitative estimation of drug-likeness (QED)** A metric designed to provide a quantitative measure of how 'drug-like' a molecule is. It essentially refers to the likelihood that a molecule possesses properties consistent with most known drugs, estimated based on a variety of molecular descriptors. We report both histograms of QED and a summary statistic in terms of the Wasserstein distance between the generated and reference distributions (smaller better).

14. **Molecular weight (Weight)** The sum of atomic weights in a molecule. We report both histograms of molecular weights and a summary statistic in terms of the Wasserstein distance between the generated and reference distributions (smaller better).